

Title:

A Novel Analytical Multilayer Cylindrical Heat Source Model for Vertical Ground Heat Exchangers Installed in Layered Ground

Author:

Aiqiang Pan^a, John S. McCartney^b, Lin Lu^{a,*}, Tian You^a

^a Department of Building Services Engineering, The Hong Kong Polytechnic University, Hong Kong, China

^b Department of Structural Engineering, University of California San Diego, 9500 Gilman Drive, La Jolla, CA 92093-0085, United States

Abstract:

This paper presents a new analytical multilayer cylindrical heat source model for vertical ground heat exchangers (GHEs) installed in layered ground using the integral-transform method. The analytical model was validated by model degradation, numerical simulation, and a laboratory-scale experiment. Results indicate that temperature profiles of vertical GHEs in layered ground are quite different from those in homogeneous ground. The temperature differences would increase with time. Also, thermal property differences between ground layers would result in additional vertical heat transfer across layer interfaces, which is not observed in homogeneous ground. This cross-layer thermal interaction is stronger when thermal property differences are larger. The role of the cylindrical heat source model was also evaluated through a comparison with a line heat source. Larger GHE thermal load, and smaller ground thermal conductivity would all lead to greater differences in the comparison. However, the error was observed to decrease with time. Therefore, it is recommended to consider the ground stratification in the design of vertical GHEs and the new multilayer cylindrical heat source model can be an effective tool for quick estimation.

Keywords:

Vertical ground heat exchangers; Layered ground; Analytical Multilayer Cylindrical heat source model; Integral transform method; Thermal interactions between layers; Laboratory-scale experiment.

Highlights

1. A new analytical heat source model for vertical GHE installed in layered ground
2. Employing the new integral-transform method to develop the analytical model
3. Extending multilayer line heat source models to the cylindrical heat source model
4. Analysis on the thermal interactions between different ground layers

Nomenclature

r'_0 dimensional radius of vertical GHE [m]

r' dimensional radial axis in cylindrical coordinate [m]

r dimensionless radial axis in cylindrical coordinate [1]

z' dimensional vertical axis in cylindrical coordinate [m]

z dimensionless vertical axis in cylindrical coordinate [1]

h' dimensional depth of disk heat source [m]

h dimensionless depth of disk heat source [1]

h'_d dimensional depth of vertical GHE [m]

h_d dimensionless depth of vertical GHE [1]

h'_i dimensional depth of soil layer [m]

h_i dimensionless depth of soil layer [1]

t' dimensional time [s]

t dimensionless time [1]

q'_z dimensional vertical heat flux [W/m²]

q_z dimensionless vertical heat flux [1]

T' dimensional temperature [K]

T dimensionless temperature [1]

Q_i thermal load per GHE length [W/m]

k_i thermal conductivity [W/(m·K)]

ρ_i density [kg/m³]

c_i specific thermal capacity $\left[J/(kg \cdot K) \right]$

α_i thermal conductivity ratio [1]

β_i thermal capacity ratio [1]

s Laplace variable

φ Hankel variable

Superscript

$^-$ Laplace transformed variable

$^=$ Hankel transformed variable

Subscript

0 reference value

i property of the corresponding ground layer

1. Introduction

1.1 Background

Ground coupled heat pump (GCHP) technology is a promising technology that can contribute to low energy buildings. As integrating energy systems on the consumer side is becoming a current trend, GCHP systems can also be effective units in the distributed energy systems [1, 2], due to the high efficiency in providing spacing cooling and heating of GCHP systems. Also, researchers recently have been studying the optimal design and control strategy of hybrid systems that integrate GCHP systems with solar energy [3, 4], as the hybrid systems may alleviate the cumulative ground thermal unbalance in heating dominant regions.

GCHP technology uses of ground as heat source or sink. Due to the more stable temperature and higher thermal capacity of ground, GCHP systems always have higher energy efficiency than traditional air source heat pumps [5]. Ground heat exchangers (GHEs) are one of the key components in GCHP systems, through which the heat carried by the circulating fluid in GHE pipes is injected into or extracted from the ground. The thermal response of GHE, representing the heat transfer performance of GHE, is hence an importance factor to the design and operation of GCHP systems [6]. In the thermal response tests (TRT) of GHE, heat source models of GHE are needed [7]. GHE heat source models are necessary for the design of GCHP systems. In the past two decades, many analytical and numerical heat transfer models for vertical GHEs have been proposed, for both conventional borehole GHEs consisting of closed-loop heat exchange pipes within a borehole backfilled with sand-bentonite grout and the new pile GHEs, or energy piles combining the pipes with pile concrete and having relatively larger diameters [8-11]. For example, Yang et al. [6] reviewed the various models for heat conduction outside and inside boreholes. Park et al. evaluated the effects of grout material on the analytical heat source solutions along with experiments and numerical simulations [12, 13]. Li et al. [14] compared the analytical models for vertical GHE with respect to time and space scales. An observation from these previous studies is

that most existing analytical models assume that the ground surrounding GHE is homogeneous, i.e., ground thermal properties are uniform. However, the real ground is always layered, especially in the context of GHEs with lengths greater than 100 m. Vertical GHEs might pass through different strata of soil or rock having large differences in thermal properties. Further, the degree of saturation of soil or rock near the ground surface may fluctuate with time, influencing the thermal properties by up to an order of magnitude [15-18]. It was also found that the saturation degree variation above the groundwater table leads to nonuniform temperature profiles with depth [19]. In the cases of layered ground, assuming a homogeneous ground may result in large errors in predicting temperature profiles of vertical GHEs [20, 21]. Although numerical models permit the consideration of multiple ground layers, analytical models provide a simpler and quicker tool to provide heat transfer information.

1.2 Experimental and numerical studies of vertical GHEs in layered ground

Recently, researchers have performed experimental studies on heat transfer processes of vertical GHEs installed in multilayered soils. For example, Li et al. [20] studied the effects of the heat transfer rate on vertical GHEs in layered subsurface and found that temperature stratification between sand and clay close to GHE could be drastic, and the difference increases with larger heat load and lower ground thermal diffusivity. Guo et al. [21] conducted a thermal response test (TRT) on a full-scale energy pile (pile GHE) in multilayered strata. The system thermal conductivity of the ground calculated through TRT with the use a homogeneous cylindrical model assuming is about 2 times larger than the values measured in the laboratory for individual soil layers. They noted that the relatively short fitting time and high heating power applied in TRT may be responsible for the error.

Some researchers also have performed numerical simulations of heat transfer processes of GHE installed multilayered soils. For example, Luo et al. [22] compared the results from two numerical models: one is homogeneous ground model using the

effective thermal conductivity, and the other is stratified model. It was found that the heat transfer amount can be differed due to different thermal and hydraulic properties of ground layers. The length of borehole GHEs can be reduced due to the lower thermal performance of the bottom layer. Florides et al. [23] studied the thermal performance of GHEs in multilayer soils numerically. They found that **the thermal energy disperses more easily in top layers for the tested cases**. So that if the substrates are sequenced in the way that top layers have higher thermal conductivity, GHEs would have better thermal performance than the case when the strata are sequenced oppositely. Therefore, it is concluded that the effect of layered subsurface on the thermal performance of GHEs cannot be neglected in analysis.

1.3 Existing analytical multilayer heat source models

With respect to analytical heat transfer models, researchers have extended the homogeneous heat source models to multilayer heat source models. Abdelaziz et al. [24] developed a multilayer line source model based on Green's function. The line heat source was divided by the boundary of each soil layer or segment. The soil segment where the point of interest is located is defined as primary segment and the other soil segments are defined as secondary segments. Firstly, by assuming that heat will only conduct radially, the thermal response by point heat sources in the primary segment is calculated, and the thermal response of secondary segments are calculated with the composite section concept. Then, the total thermal response is obtained by summing up the contributions from primary and secondary segments. Finally, the solutions are adjusted by using a two-layer composite section to account for interlayer heat transfer due to vertical temperature gradients. Using the same principle, Erol et al. [25] extended the multilayer line heat source model to consider groundwater seepage. **The analytical heat source models considering groundwater seepage may induce significant errors as the borehole diameter becomes larger [26]**. The effects of impermeable materials of grout on analytical solutions of the heat transfer model may also need to be considered

[27]. Hu [28] also provided a line heat source model for borehole GHE in multilayer substrates with groundwater flow. His model is also based on the linear superposition principle. The line heat source is firstly divided by the boundary of soil layers, and then effects of each divided line heat source are added up. However, Hu [28] simplified the calculation that when integrating the point heat source (Green's function) in each layer, the thermal properties of other soil layers are considered as the same as the layer where the point heat source is being integrated.

In summary, the existing analytical multilayer line heat source models for GHE in multilayer soils were generally based on the Green's function method. And all these multilayer line heat source models involve some certain assumptions in model derivations as we described above: simplifying the actual axial heat transfer across ground layers or neglecting it. Also, obviously, the multilayer heat source models mentioned above consider vertical GHE as a line heat source. However, the line heat source models might only be acceptable for borehole GHE that are small enough in radius and long enough in depth. It is not accurate for vertical GHE which are relatively larger in radius or shorter in depth. On the other hand, while homogeneous cylindrical heat source models for vertical GHE have been developed, the development of multilayer cylindrical heat source models for vertical GHE is very limited.

In view of this, Zhou et al. [29] extended the solid cylindrical and the ring-coil heat source model for pile GHE in a double-layered ground using Green's function method and variable separation technique. The model derivations involve the constrained Newton method to solve nonlinear eigenvalues equations. Their model was validated by model degradation (setting the same thermal properties for two soil layers in their model), and then comparing the results with the existing solid cylindrical heat source model proposed by Man et al. [30]. However, it might not be feasible to further extend the model for PGHE installed in ground soil with more than two layers.

Therefore, this paper aims to develop a new analytical multilayer heat source model that considers vertical GHE as a cylinder heat source, rather than a line heat

source. Instead of being based on Green's function method, the integral-transform method is newly employed. The integral transform method is especially suitable for addressing the issue of the layered ground and permits rapid calculations. More importantly, the model derivation involves no assumption on the nature of heat transfer (e.g. radial heat transfer only), a limitation of existing analytical multilayer line heat source models. Using the newly developed analytical multilayer cylindrical heat source model, temperature profiles of vertical GHE in homogeneous and inhomogeneous ground are compared. The vertical heat fluxes through soil layer interface, i.e., thermal interactions between soil layers are also investigated. Moreover, the error of using multilayer line heat model to predict temperature response of vertical GHE is analyzed by comparing with the results of the new multilayer cylindrical heat source model.

2. Model development

2.1 Assumptions

A schematic of a vertical GHE installed in layered ground is shown in Figure 1. The vertical GHE is considered as a cylindrical heat source, which passes through several ground layers. The initial temperature of the ground is assumed to be uniform. The temperature of ground surface is assumed to be the same as initial temperature and remain constant. These assumptions are common when developing analytical heat transfer models for vertical GHEs used in engineering practice [30]. Also, the existing “solid” cylindrical heat source model assumes that heat flux evenly distributes on the cylindrical surface [30]. In this paper, the cylindrical heat source is divided into numerous disk heat sources overlapping along the depth of vertical GHE. This method of treating the cylindrical heat source is related with the layered ground and the integral-transform method that this paper employed to develop the multilayer cylindrical heat source model. The details of model derivation are presented in the following sections.

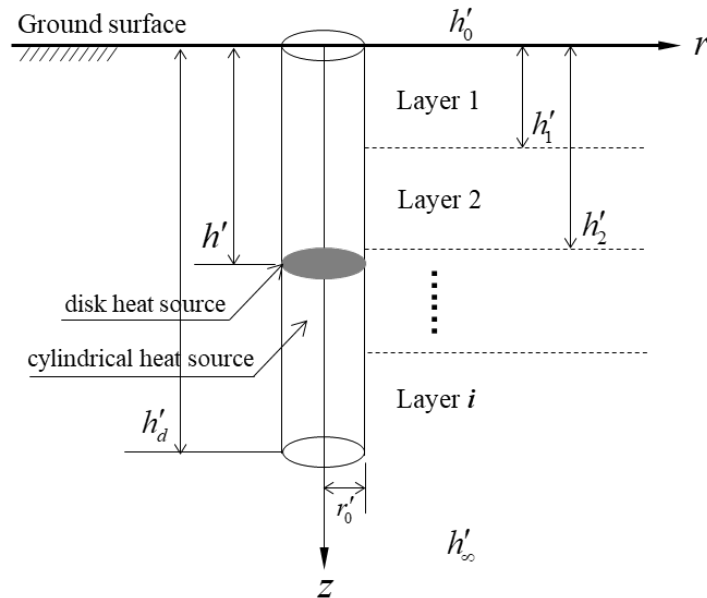


Figure 1 The schematic of vertical GHE in layered ground

2.2 Pretreatments on heat transfer equations

The model development starts from the basic heat conduction equation:

$$\rho_i c_i \frac{\partial T'}{\partial t'} = k_i \left(\frac{\partial^2 T'}{\partial r'^2} + \frac{1}{r'} \frac{\partial T'}{\partial r'} + \frac{\partial^2 T'}{\partial z'^2} \right) \quad (1)$$

The subscript i denotes variables in the corresponding soil layer. The superscript ' denotes the dimensional variables.

As shown in Figure 1, each separate soil layer contains the “partial” cylindrical heat source in that layer between the upper and lower boundaries. If the temperature and heat flux on the upper and lower boundary of each soil layer are determined, then the temperature in each soil layer can be determined. Staring from this idea, the vertical heat flux $q'_z = -k_i \frac{\partial T'}{\partial z'}$ is introduced into the model derivation for determining the heat flux on soil layer interfaces. With the vertical heat flux, Equation (1) can be rewritten in the following set of equations:

$$\begin{aligned} \frac{\partial T'}{\partial z'} &= -\frac{1}{k_i} q'_z \\ \frac{\partial q'_z}{\partial z'} &= k_i \left(\frac{\partial^2 T'}{\partial r'^2} + \frac{1}{r'} \frac{\partial T'}{\partial r'} \right) - \rho_i c_i \frac{\partial T'}{\partial t'} \end{aligned} \quad (2)$$

According to the assumptions mentioned above, the initial condition, and boundary conditions of the ground are:

$$T'(r', z', 0) = T'_0 \quad (3)$$

$$T'(r', 0, t') = T'_0 \quad (4)$$

$$T'(r', \infty, t') = T'_0 \quad (5)$$

Also, as mentioned above that the cylindrical heat source is divided into numerous disk heat sources, the expression of a disk heat source is:

$$q'_{zs} = \frac{Q_l}{\pi r_0'^2} dh' \quad (0 \leq h' \leq h'_d) \quad (6)$$

where Q_l is the thermal load per length of vertical GHE (W/m), dh' is the differential of the cylindrical heat source.

The following dimensionless variables can be defined:

$$r = \frac{r'}{r'_0} \quad (7)$$

$$z = \frac{z'}{r'_0} \quad (8)$$

$$h = \frac{h'}{r'_0} \quad (9)$$

$$h_d = \frac{h'_d}{r'_0} \quad (10)$$

$$t = \frac{k_0 t'}{\rho_0 c_0 r_0'^2} \quad (11)$$

$$T = \frac{k_0 (T' - T'_0)}{Q_l} \quad (12)$$

$$q_z = \frac{r'_0}{Q_l} q'_z \quad (13)$$

$$\alpha_i = \frac{k_i}{k_0} \quad (14)$$

$$\beta_i = \frac{\rho_i c_i}{\rho_0 c_0} \quad (15)$$

Using these variables, Equations (2) to (6) can be nondimensionalized to form Equations (16) to (20) respectively.

$$\frac{\partial T}{\partial z} = -\frac{1}{\alpha_i} q_z \quad (16)$$

$$\frac{\partial q_z}{\partial z} = \alpha_i \left(\frac{\partial^2 T}{\partial r^2} + \frac{1}{r} \frac{\partial T}{\partial r} \right) - \beta_i \frac{\partial T}{\partial t}$$

$$T(r, z, 0) = 0 \quad (17)$$

$$T(r, 0, t) = 0 \quad (18)$$

$$T(r, \infty, t) = 0 \quad (19)$$

$$q_{zs} = \frac{dh}{\pi} \quad (0 \leq r \leq 1, 0 \leq h \leq h_d) \quad (20)$$

The definition of Laplace transform is $L[F(t)] = \bar{F}(s) = \int_0^\infty e^{-st} F(t) dt$, where s is Laplace variable. Writing Equation (16) in matrix form and applying Laplace transform on time t using the Laplace transform property: $L[\frac{\partial}{\partial t} F(t)] = s\bar{F}(s) - F(+0)$ results in the following equation:

$$\frac{\partial}{\partial z} \begin{pmatrix} \bar{T}(r, z, s) \\ \bar{q}_z(r, z, s) \end{pmatrix} = \begin{pmatrix} 0 & -\frac{1}{\alpha_i} \\ \alpha_i \left(\frac{\partial^2}{\partial r^2} + \frac{1}{r} \frac{\partial}{\partial r} \right) - \beta_i s & 0 \end{pmatrix} \begin{pmatrix} \bar{T}(r, z, s) \\ \bar{q}_z(r, z, s) \end{pmatrix} \quad (21)$$

The definition of Hankel transform is $H[F(r)] = \bar{\bar{F}}(\varphi) = \int_0^\infty r J_0(\varphi r) F(r) dr$, where $J_0(x)$ is 0-order first kind Bessel function: $J_0(x) = \frac{1}{\pi} \int_0^\pi e^{ix \cos \theta} d\theta = \frac{1}{\pi} \int_0^\pi \cos(x \sin \theta) d\theta$ and φ is Hankel variable.

The Hankel transform is then applied on Equation (21) with respect to r using the property that for $\lim_{x \rightarrow \infty} F(x) = 0$, $H[\frac{\partial^2 F(x)}{\partial r^2} + \frac{1}{r} \frac{\partial F(x)}{\partial r}] = -\varphi^2 H[F(x)] = -\varphi^2 \bar{\bar{F}}(\varphi)$ [31], resulting in:

$$\frac{d}{dz} \begin{pmatrix} \bar{\bar{T}}(\varphi, z, s) \\ \bar{\bar{q}}_z(\varphi, z, s) \end{pmatrix} = \begin{pmatrix} 0 & -\frac{1}{\alpha_i} \\ -\alpha_i \varphi^2 - \beta_i s & 0 \end{pmatrix} \begin{pmatrix} \bar{\bar{T}}(\varphi, z, s) \\ \bar{\bar{q}}_z(\varphi, z, s) \end{pmatrix} \quad (22)$$

$$\text{Letting } \bar{\bar{X}}(\varphi, z, s) = \begin{pmatrix} \bar{\bar{T}}(\varphi, z, s) \\ \bar{\bar{q}}_z(\varphi, z, s) \end{pmatrix}, \quad \bar{\bar{A}}_i(\varphi, s) = \begin{pmatrix} 0 & -\frac{1}{\alpha_i} \\ -\alpha_i \varphi^2 - \beta_i s & 0 \end{pmatrix}, \text{ Equation (22)}$$

can be rewritten as:

$$\frac{d}{dz} \bar{\bar{X}}(\varphi, z, s) = \bar{\bar{A}}_i(\varphi, s) \bar{\bar{X}}(\varphi, z, s) \quad (23)$$

Equation (23) is an ordinary differential equation of the first order. The general solution of this equation is:

$$\bar{\bar{X}}(\varphi, z, s) = \exp[\bar{\bar{A}}_i(\varphi, s) \cdot (z - h_{i-1})] \bar{\bar{X}}(\varphi, h_{i-1}, s) \quad (24)$$

h_{i-1} is the depth of each soil layer ($h_0 = 0$). $\exp[\bar{\bar{A}}_i(\varphi, s) \cdot (z - h_{i-1})]$ can be calculated with $a_i I + b_i \bar{\bar{A}}_i(\varphi, s)$ according to Cayley-Hamilton theorem [32]. The two eigenvalues of matrix $\bar{\bar{A}}_i(\varphi, s)$ can be obtained by solving its proper equation, which gives $\gamma_{1,2} = \pm \sqrt{\varphi^2 + \frac{\beta_i}{\alpha_i} s} = \pm \gamma_i$. The two coefficients a_i, b_i can be determined as follows.

$$\begin{aligned} a_i &= \frac{\exp[\gamma_i(z - h_{i-1})] + \exp[-\gamma_i(z - h_{i-1})]}{2} \\ b_i &= \frac{\exp[\gamma_i(z - h_{i-1})] - \exp[-\gamma_i(z - h_{i-1})]}{2\gamma_i} \end{aligned} \quad (25)$$

Let $B_i(\varphi, z - h_{i-1}, s)$ denotes $\exp[\bar{\bar{A}}_i(\varphi, s) \cdot (z - h_{i-1})]$, for each soil layer, the general solution is

$$\bar{\bar{X}}(\varphi, z, s) = B_i(\varphi, z - h_{i-1}, s) \bar{\bar{X}}(\varphi, h_{i-1}, s) \quad (26)$$

where $B_i(\varphi, z - h_{i-1}, s) = \begin{bmatrix} a_i & -\frac{b_i}{\alpha_i} \\ -\alpha_i \gamma_i^2 b_i & a_i \end{bmatrix}$.

Also, the disk heat source in Equation (20) after Laplace and Hankel transform is

$$\frac{J_1(\varphi) dh}{\pi \varphi s} \quad (\text{the property of Laplace transform } F(t) = 1, L[1] = \frac{1}{s} \text{ and Hankel transform}$$

$$F(r) = 1, \int_0^x r J_0(\varphi r) dr = \frac{x J_1(x \varphi)}{\varphi} \text{ have been utilized}).$$

2.3 Derivation of multilayer cylindrical heat source model

The model derivation for vertical GHE surrounded by two ground layers is presented as a case to demonstrate the model derivation procedure. The model can certainly be extended to a specific number of soil layers according to practical applications. The example extending the model to three-layer ground is presented in Appendix A.

The entire cylindrical heat source in the two-layer ground is firstly separated into two cylindrical heat sources according to the boundaries of ground layers as shown in Figure 2. Each separated cylindrical heat source composes of numerous disk heat sources. Firstly, solution for each separated cylindrical heat source will be derived. Then, solution of the entire cylindrical heat source will be obtained by adding up the solution of each separated cylindrical heat sources.

The solution derivation for each separated cylindrical heat source undergoes the same three steps. Step 1: deriving vertical heat flux and temperature on all the ground layer boundaries. Step 2: deriving the temperature solutions of disk heat source in all ground layers. Step 3: integrating the solutions of disk heat source along the depth of each separated cylindrical heat source to get the solutions of each separated cylindrical heat source in all ground layers.

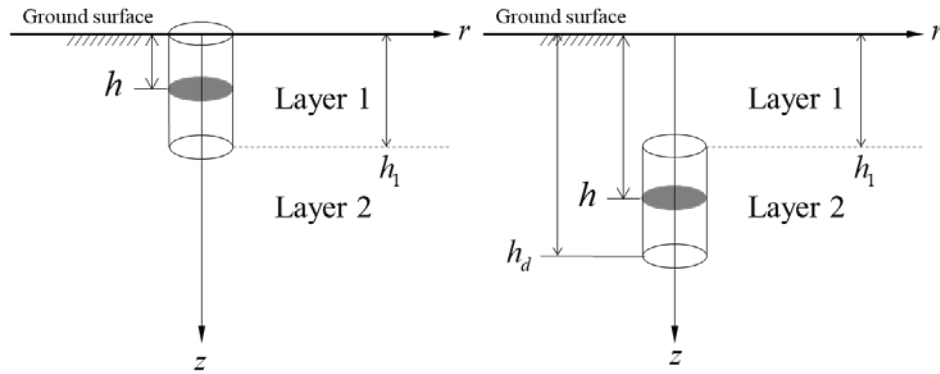


Figure 2 The separated cylindricval heat source in each soil layer

For the separated cylindrical heat source in layer 1 (Figure 2), the range of disk heat source is $0 < h < h_1$.

Step 1: solving for heat flux and temperature on boundaries: $\bar{\bar{q}}_z(\varphi, 0, s)$, $\bar{\bar{T}}(\varphi, h_1, s)$, $\bar{\bar{q}}_z(\varphi, h_1, s)$

According to Equation (26), at $z = \infty$

$$\bar{\bar{T}}(\varphi, \infty, s) = (a_2)_{\infty} \bar{\bar{T}}(\varphi, h_1, s) - \left(\frac{b_2}{\alpha_2} \right)_{\infty} \bar{\bar{q}}_z(\varphi, h_1, s) \quad (27)$$

The subscript outside the parenthesis denotes the value of z inside the parenthesis and

so does the followings. With boundary conditions, Equation (27) gives:

$$\alpha_2 \gamma_2 \bar{\bar{T}}(\varphi, h_1, s) = \bar{\bar{q}}_z(\varphi, h_1, s) \quad (28)$$

Also, at $z = h_1$

$$\begin{aligned} \bar{\bar{T}}(\varphi, h_1, s) &= -\left(\frac{b_1}{\alpha_1}\right)_{h_1} \bar{\bar{q}}_z(\varphi, 0, s) - \frac{J_1(\varphi)dh}{\pi\varphi s} \left(\frac{b_1}{\alpha_1}\right)_{h_1-h} \\ \bar{\bar{q}}_z(\varphi, h_1, s) &= (a_1)_{h_1} \bar{\bar{q}}_z(\varphi, 0, s) + \frac{J_1(\varphi)dh}{\pi\varphi s} (a_1)_{h_1-h} \end{aligned} \quad (29)$$

With Equations (28) and (29), $\bar{\bar{q}}_z(\varphi, 0, s)$ can be obtained:

$$\bar{\bar{q}}_z(\varphi, 0, s) = -C_1 \frac{J_1(\varphi)dh}{\pi\varphi s} \quad (30)$$

where $C_1 = \frac{\alpha_2 \gamma_2 \left(\frac{b_1}{\alpha_1}\right)_{h_1-h} + (a_1)_{h_1-h}}{\alpha_2 \gamma_2 \left(\frac{b_1}{\alpha_1}\right)_{h_1} + (a_1)_{h_1}}$. And $\bar{\bar{T}}(\varphi, h_1, s), \bar{\bar{q}}_z(\varphi, h_1, s)$ can also be obtained

respectively.

$$\begin{aligned} \bar{\bar{T}}(\varphi, h_1, s) &= \left[\left(\frac{b_1}{\alpha_1}\right)_{h_1} C_1 - \left(\frac{b_1}{\alpha_1}\right)_{h_1-h} \right] \frac{J_1(\varphi)dh}{\pi\varphi s} \\ \bar{\bar{q}}_z(\varphi, h_1, s) &= \left[-(a_1)_{h_1} C_1 + (a_1)_{h_1-h} \right] \frac{J_1(\varphi)dh}{\pi\varphi s} \end{aligned} \quad (31)$$

Step 2: solutions of disk heat source in all layers

Using the solution of $\bar{\bar{q}}_z(\varphi, 0, s), \bar{\bar{T}}(\varphi, h_1, s), \bar{\bar{q}}_z(\varphi, h_1, s)$, the solution of disk heat source in each layer can be obtained. According to Equation (26), in layer 1 ($0 < z < h_1$)

For $z < h < h_1$

$$\bar{\bar{T}}(\varphi, z, s) = \frac{b_1}{\alpha_1} C_1 \frac{J_1(\varphi)dh}{\pi\varphi s} \quad (32)$$

For $h < z < h_1$

$$\bar{\bar{T}}(\varphi, z, s) = \left[\frac{b_1}{\alpha_1} C_1 - \left(\frac{b_1}{\alpha_1} \right)_{z-h} \right] \frac{J_1(\varphi) dh}{\pi \varphi s} \quad (33)$$

In layer 2 ($h_1 < z$)

$$\bar{\bar{T}}(\varphi, z, s) = \left\{ a_2 \left[\left(\frac{b_1}{\alpha_1} \right)_{h_1} C_1 - \left(\frac{b_1}{\alpha_1} \right)_{h_1-h} \right] - \frac{b_2}{\alpha_2} \left[-(a_1)_{h_1} C_1 + (a_1)_{h_1-h} \right] \right\} \frac{J_1(\varphi) dh}{\pi \varphi s} \quad (34)$$

Step 3: solutions of separated cylindrical heat source

For $0 < z < h_1$, adding up integration of Equation (33) from 0 to z and Equation (32)

from z to h_1 , and the result is:

$$\bar{\bar{T}}(\varphi, z, s) = \frac{\left[(1-a_1)(a_1)_{h_1} + b_1(b_1)_{h_1} \gamma_1^2 \right] \alpha_1 + \left[b_1(a_1)_{h_1} + (1-a_1)(b_1)_{h_1} - b_1 \right] \gamma_2 \alpha_2}{\alpha_1 \gamma_1^2 \left[\alpha_1(a_1)_{h_1} + \alpha_2 \gamma_2(b_1)_{h_1} \right]} \frac{J_1(\varphi)}{\pi \varphi s} \quad (35)$$

For $h_1 < z$, integrating Equation (34) from 0 to h_1 gives:

$$\bar{\bar{T}}(\varphi, z, s) = \frac{\exp[-\gamma_2(z-h_1)] \left[-1 + (a_1)_{h_1} \right] J_1(\varphi)}{\left[\alpha_2 \gamma_2(b_1)_{h_1} + \alpha_1(a_1)_{h_1} \right] \gamma_1^2} \frac{J_1(\varphi)}{\pi \varphi s} \quad (36)$$

For the separated cylindrical heat source in layer 2 (Figure 2), the range of disk heat source is $h_1 < h < h_d$.

Step 1: solving for heat flux and temperature on boundaries: $\bar{\bar{q}}_z(\varphi, 0, s)$, $\bar{\bar{T}}(\varphi, h_1, s)$,

$$\bar{\bar{q}}_z(\varphi, h_1, s)$$

According to Equation (26), at $z = \infty$

$$\bar{\bar{T}}(\varphi, \infty, s) = (a_2)_{\infty} \bar{\bar{T}}(\varphi, h_1, s) - \left(\frac{b_2}{\alpha_2} \right)_{\infty} \bar{\bar{q}}_z(\varphi, h_1, s) - \frac{J_1(\varphi) dh}{\pi \varphi s} \left(\frac{b_2}{\alpha_2} \right)_{\infty-h} \quad (37)$$

With boundary conditions, it gives:

$$0 = -\alpha_2 \gamma_2 \bar{\bar{T}}(\varphi, h_1, s) + \bar{\bar{q}}_z(\varphi, h_1, s) + \frac{J_1(\varphi) dh}{\pi \varphi s} \exp(-\gamma_2 h) \quad (38)$$

Also, at $z = h_1$

$$\begin{aligned}\bar{\bar{T}}(\varphi, h_1, s) &= -\left(\frac{b_1}{\alpha_1}\right)_{h_1} \bar{\bar{q}}_z(\varphi, 0, s) \\ \bar{\bar{q}}_z(\varphi, h_1, s) &= (a_1)_{h_1} \bar{\bar{q}}_z(\varphi, 0, s)\end{aligned}\quad (39)$$

With Equations (38) and (39), $\bar{\bar{q}}_z(\varphi, 0, s)$ can be obtained:

$$\bar{\bar{q}}_z(\varphi, 0, s) = -C_2 \frac{J_1(\varphi)dh}{\pi\varphi s} \quad (40)$$

where $C_2 = \frac{\exp(-\gamma_2 h)}{(a_1)_{h_1} + \alpha_2 \gamma_2 \left(\frac{b_1}{\alpha_1}\right)_{h_1}}$. And $\bar{\bar{T}}(\varphi, h_1, s), \bar{\bar{q}}_z(\varphi, h_1, s)$ can also be obtained

respectively.

$$\begin{aligned}\bar{\bar{T}}(\varphi, h_1, s) &= \left(\frac{b_1}{\alpha_1}\right)_{h_1} C_2 \frac{J_1(\varphi)dh}{\pi\varphi s} \\ \bar{\bar{q}}_z(\varphi, h_1, s) &= -(a_1)_{h_1} C_2 \frac{J_1(\varphi)dh}{\pi\varphi s}\end{aligned}\quad (41)$$

Step 2: solutions of disk heat source in all layers

Using the solution of $\bar{\bar{q}}_z(\varphi, 0, s), \bar{\bar{T}}(\varphi, h_1, s), \bar{\bar{q}}_z(\varphi, h_1, s)$, the solution of disk heat source in each layer can be obtained. According to Equation (26), in layer 1 ($0 < z < h_1$)

$$\bar{\bar{T}}(\varphi, z, s) = \frac{b_1}{\alpha_1} C_2 \frac{J_1(\varphi)dh}{\pi\varphi s} \quad (42)$$

In layer 2 ($h_1 < z$)

For $h_1 < z < h$

$$\bar{\bar{T}}(\varphi, z, s) = \left\{ a_2 \left(\frac{b_1}{\alpha_1}\right)_{h_1} C_2 + \frac{b_2}{\alpha_2} (a_1)_{h_1} C_2 \right\} \frac{J_1(\varphi)dh}{\pi\varphi s} \quad (43)$$

For $h < z$

$$\bar{\bar{T}}(\varphi, z, s) = \left\{ a_2 \left(\frac{b_1}{\alpha_1}\right)_{h_1} C_2 + \frac{b_2}{\alpha_2} (a_1)_{h_1} C_2 - \left(\frac{b_2}{\alpha_2}\right)_{z-h} \right\} \frac{J_1(\varphi)dh}{\pi\varphi s} \quad (44)$$

Step 3: solutions of separated cylindrical heat source

For $0 < z < h_1$, integrating Equation (42) from 0 to $h_d - h_1$ gives:

$$\frac{b_1 [1 - \exp[-\gamma_2(h_d - h_1)]]}{\alpha_1 \gamma_2 (a_1)_{h_1} + \alpha_2 \gamma_2^2 (b_1)_{h_1}} \quad (45)$$

For $h_1 < z < h_d$, adding up integration of Equation (44) from 0 to $z - h_1$ and Equation (43) from $z - h_1$ to $h_d - h_1$, and the result is:

$$\frac{-\gamma_2 [\alpha_1 b_2 (a_1)_{h_1} + \alpha_2 a_2 (b_1)_{h_1}] \exp[-\gamma_2(h_d - h_1)] + \gamma_2 [\alpha_1 b_2 (a_1)_{h_1} + \alpha_2 (b_1)_{h_1}] - \alpha_1 (a_1)_{h_1} (a_2 - 1)}{\alpha_2 \gamma_2^2 [\alpha_2 \gamma_2 (b_1)_{h_1} + \alpha_1 (a_1)_{h_1}]} \quad (46)$$

The solution of the entire cylindrical heat source can be obtained by adding up the solutions in each layer by the two separated cylindrical heat sources, as shown in Figure 3. For $0 < z < h_1$, adding up Equations (35) and (45). For $h_1 < z < h_d$, adding up Equations (36) and (46).

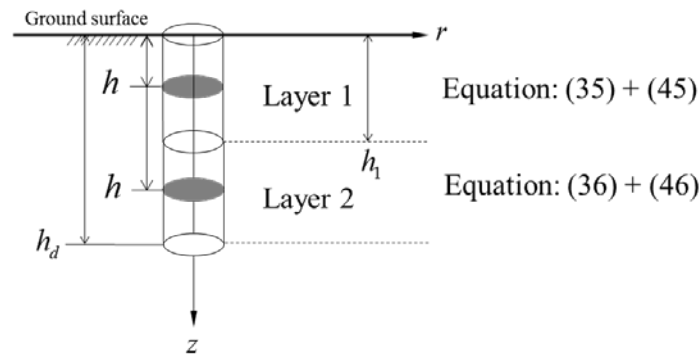


Figure 3 Solution of assembled cylindrical heat source

The solution equations contain the Laplace variable and Hankel variable. To obtain the solution in physical domain, the solution equations need to be converted. Due to the complexity of the solution equations, it is difficult to find analytical inversions. Numerical inversion methods were chosen to accomplish the inversion process. Two different numerical inverse Laplace transforms methods [33, 34] and two different numerical inverse Hankel transforms methods [35, 36] were adopted

respectively. Adopting either combination of the numerical inversion methods yields the same result, so that the result can be believed to be independent of inversion method. The calculation process typically requires one or two minutes.

3 Model validation

The model was validated in three ways: degrading the model to the case of homogeneous ground and comparing its results with an established homogeneous cylindrical heat transfer model; comparing the results of the analytical multilayer cylindrical heat source soil model with that of numerical simulations, and comparing with the results of a laboratory-scale experiment.

3.1 Model degradation

For homogeneous soil, the thermal conductivity and specific thermal capacity in the solution equations would be identical, i.e.: $\alpha_1 = \alpha_2 = 1$, $\beta_1 = \beta_2 = 1$ and $\gamma_1 = \gamma_2 = \gamma = \sqrt{\varphi^2 + s}$. And obviously, the sum of Equations (35) and (45), and the sum of Equations (36) and (46) should give the same expression. The degradation results of Equations (35), (36), (45), and (46) are the following equations respectively:

$$\bar{\bar{T}}(\varphi, z, s) = [1 - \exp(-\gamma z) - \exp(-\gamma h_1) \gamma b_1] \frac{J_1(\varphi)}{\pi \varphi s \gamma^2} \quad (47)$$

$$\bar{\bar{T}}(\varphi, z, s) = \exp(-\gamma z) \left[(a_1)_{h_1} - 1 \right] \frac{J_1(\varphi)}{\pi \varphi s \gamma^2} \quad (48)$$

$$\bar{\bar{T}}(\varphi, z, s) = [-\exp(-\gamma h_d) + \exp(-\gamma h_1)] \gamma b_1 \frac{J_1(\varphi)}{\pi \varphi s \gamma^2} \quad (49)$$

$$\bar{\bar{T}}(\varphi, z, s) = [1 - \exp(-\gamma z) (a_1)_{h_1} - \exp(-\gamma h_d) \gamma b_1] \frac{J_1(\varphi)}{\pi \varphi s \gamma^2} \quad (50)$$

Obviously, the sum of Equations (47) and (49), and the sum of Equations (48) and (50) give the same result:

$$\bar{\bar{T}}(\varphi, z, s) = \frac{J_1(\varphi)}{\pi \varphi s \gamma^2} [1 - \exp(-\gamma z) - \exp(-\gamma h_d) \gamma b_1] \quad (51)$$

The results calculated with Equation (51) should almost be the same as the existing homogeneous cylindrical heat source model. The cylindrical heat source model by Man

et al. [30] is selected as the reference model. Comparison of the dimensionless

temperature ($T = \frac{k_0(T' - T'_0)}{Q_l}$) at different dimensionless time ($t = \frac{k_0 t'}{\rho_0 c_0 r_0'^2}$) on vertical

GHE wall ($r=1$) with dimensionless depth of 100 ($z = \frac{z'}{r_0'}$) are shown in Figure 4.

Temperature solutions calculated by degraded multilayer model and the homogeneous model agree well, except for very limited error at the beginning. This error is believed to be related with the different treatment of heat source: heat is released from the cylindrical surface in Man et al.'s model, whereas the cylindrical heat source is considered as a solid heat “rod” in the new multilayer model.

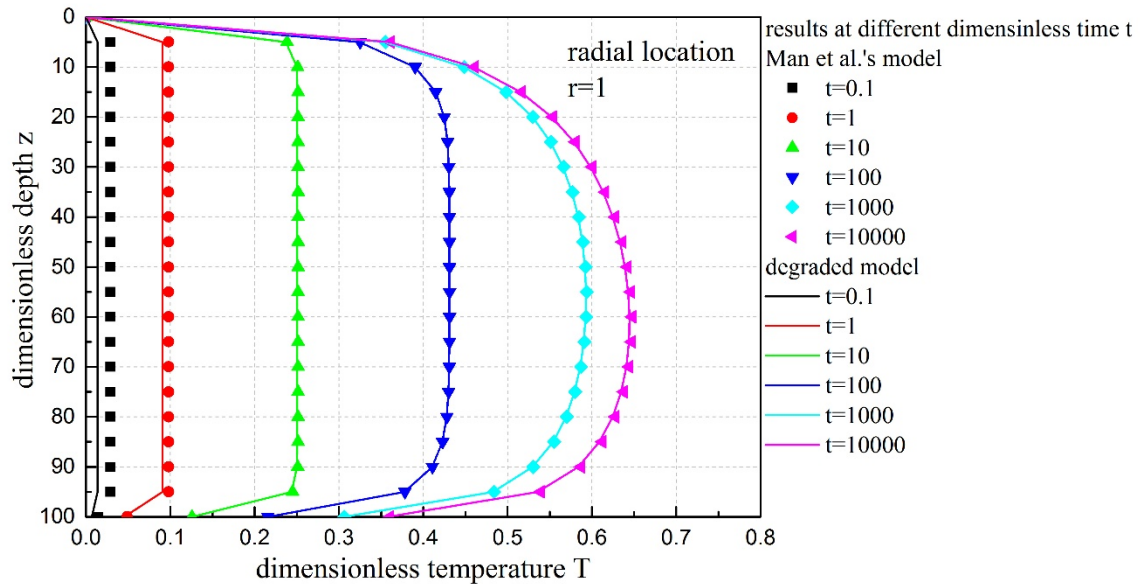
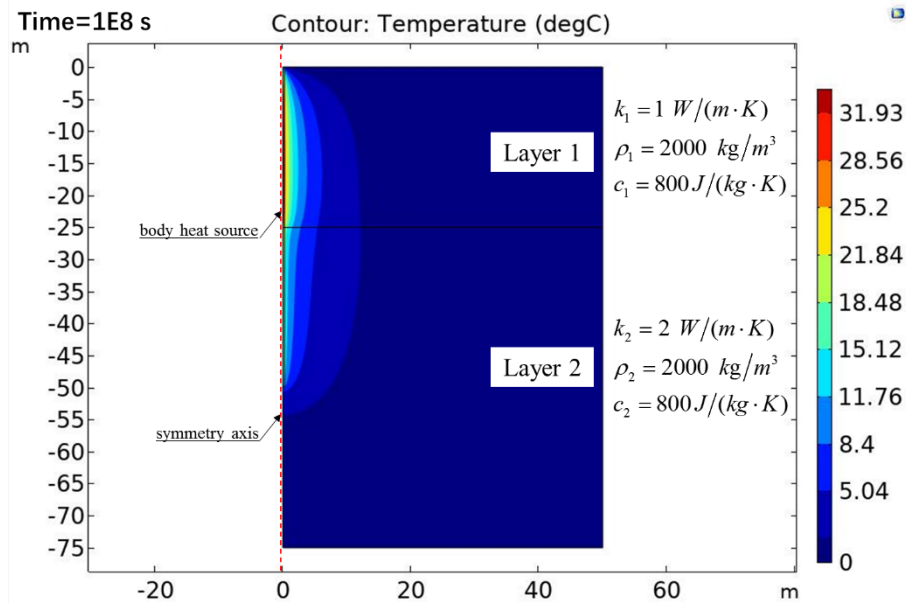


Figure 4 Comparison between degraded and homogeneous model

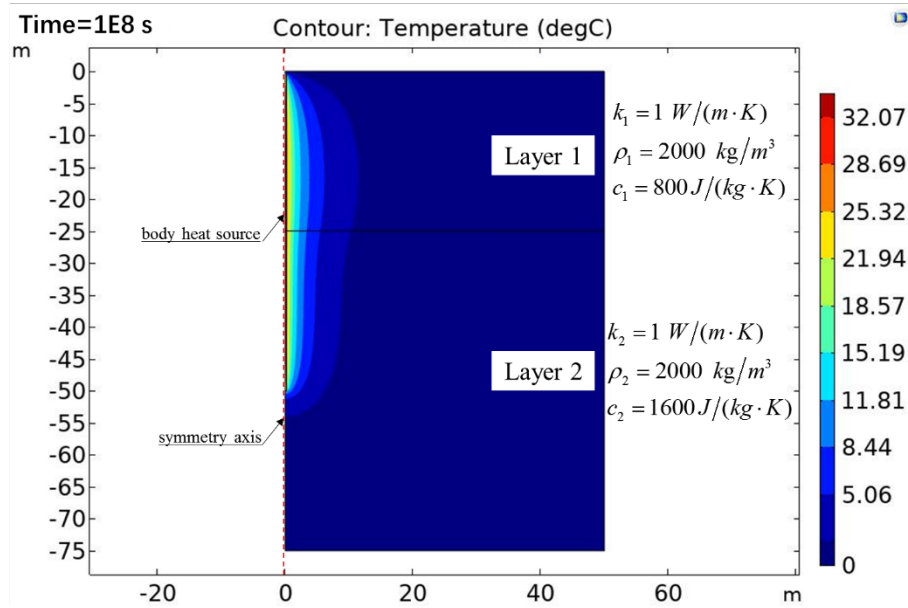
3.2 Numerical simulation

The results of the multilayer cylindrical heat source model were also compared with those of numerical simulation for validation purpose. The numerical simulation was conducted using COMSOL Multiphysics, assuming heat transfer by conduction only. The physical model in numerical simulation is 2D axisymmetric. Two simulation cases are shown in Figure 5. The cylindrical heat source is 50 m deep with a radius of

0.25 m, and the simulation domain is a cylinder 75 m in height and 50 m in radius. This domain was verified to be large enough within the simulated time ranged that applying either fixed temperature boundary conditions or insulation boundary conditions on domain boundaries gives the same results. The vertical GHE is defined as a body heat source in the numerical simulations, and the thermal load of vertical GHE is 50 W/m . The ground is considered as two layers with different thermal properties. Upper layer (layer 1) is 25 m deep and below is layer 2. For simulation case 1, thermal conductivity of layer 1 and layer 2 is $1 \text{ W/(m} \cdot \text{K)}$ and $2 \text{ W/(m} \cdot \text{K)}$ respectively, and density and thermal capacity in simulation case 1 are set to be the same. For simulation case 2, thermal capacity of layer 1 and layer 2 is $800 \text{ J/(kg} \cdot \text{K)}$ and $1600 \text{ J/(kg} \cdot \text{K)}$ respectively, and thermal conductivity and density in simulation case 2 are set to be the same.



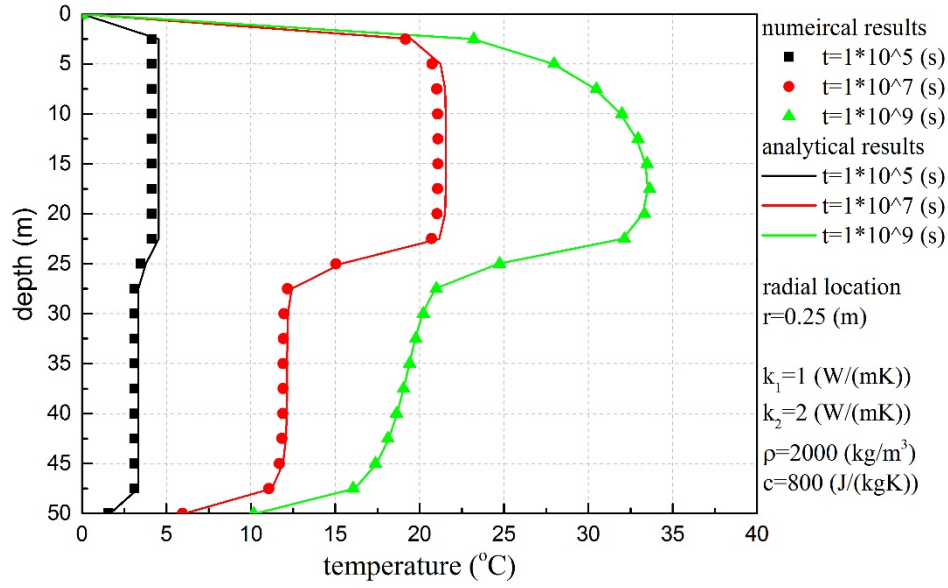
(a) Case 1: different thermal conductivities



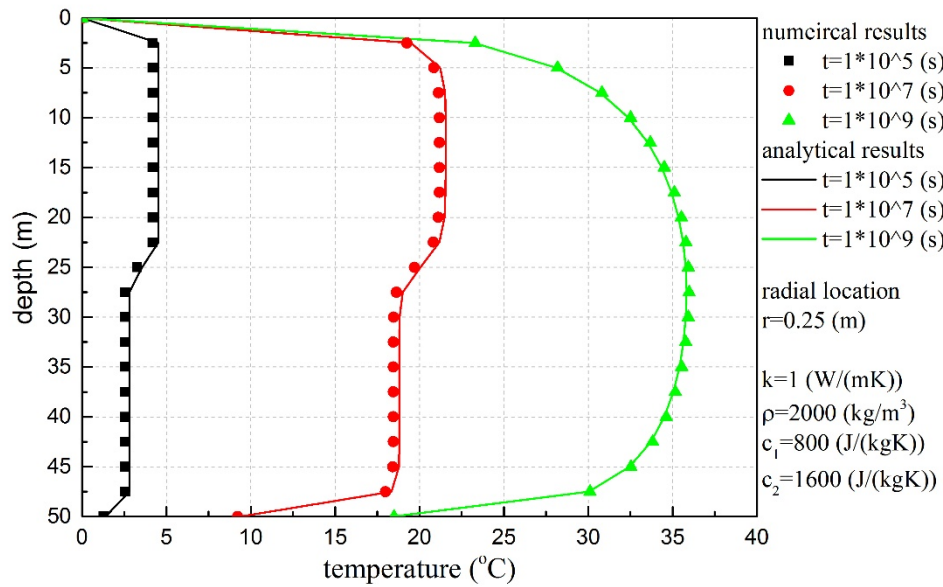
(b) Case 2: different thermal capacities

Figure 5 Numerical simulation cases using COMSOL

The dimensionless temperature solutions calculated with the multilayer cylindrical heat transfer model were converted to dimensional temperature solutions using the parameters values defined in numerical simulations. The comparisons of numerical and analytical results for the two cases are shown in Figure 6. Clearly, the results of multilayer cylindrical heat source model and that of numerical simulations match well. The temperature differences due to different thermal conductivities increase with time. In contrast, the temperature differences caused by different thermal capacities would vanishes in the long term. The reason why the thermal conductivity and the thermal capacity have different effect on ground temperature change is explained in chapter 4.



(a) comparison under different thermal conductivities



(b) comparison under different thermal capacities

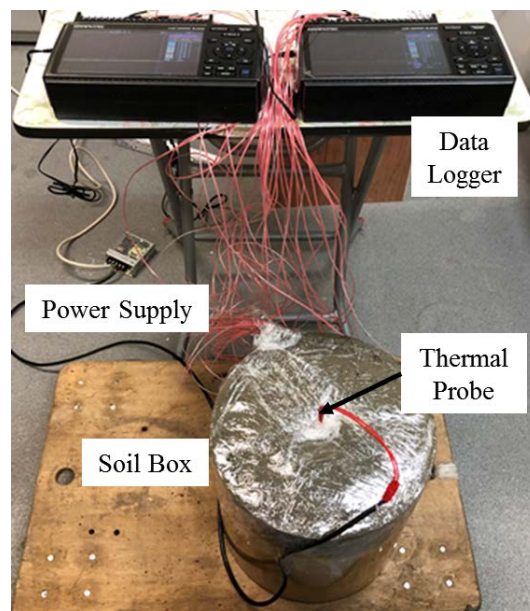
Figure 6 Comparisons of numerical and analytical models

3.3 Laboratory-scale experiment

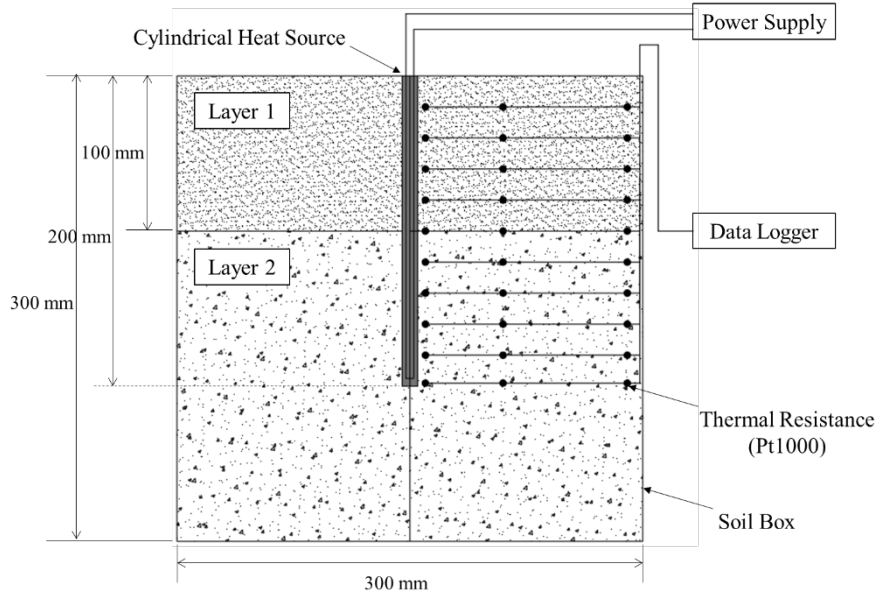
A Laboratory-scale experiment of a cylindrical heat source buried in two soil layers was conducted. The experimental rig is shown in Figure 7 (a). The schematic diagram of the soil layer arrangement, the cylindrical heat source, and resistance thermometers (Pt 1000) are shown in Figure 7 (b). The soil box is cylinder made of 5

mm thick acrylic material. The inner sizes of the soil box is 300 mm in height and 300 mm in diameter. The custom-made thermal probe, functioning as the cylindrical heat source, is 200 mm long and 6 mm in diameter. It was made of alloy resistance wire uniformly coiled (tightly wrapped) around a metal cylinder and covered with stainless steel tube. The resistance of the thermal probe was measured to be $171.1 \, \Omega$. The power supply was 16 V direct current. So that the heat rate of the thermal probe is $7.48 \, W/m$.

The thermal probe was inserted in the middle of soil box. Soil layer 1 (silt) was 100 mm thick, and below (200 mm thick) was the soil layer 2 (sand). The depth of soil is half length deeper than the length of thermal probe to avoid the bottom boundary effect on temperature in the short term experiment. To avoid possible thermally induced moisture migration during the experiment, the silt and sand were saturated. There were three columns of resistance thermometers, the distance between the three columns and the central axis of the cylindrical soil box was 10 mm, 60 mm, and 140 mm respectively. The reason for the vertical arrangement of the resistance thermometers was to measure the vertical temperature profiles across the soil layers.



(a) Experimental rig



(b) Schematic diagram

Figure 7 Laboratory-scale experiment of cylindrical heat source in a double layered soil deposits

To compare the experimental data with the analytical solution, the bulk density, thermal properties of the two soil layers need to be obtained. The cutting ring method was used to measure the soil bulk density following the standard ASTM D7263-09. The test rig for measuring soil thermal conductivity is shown in Figure 8. The rig (TC3000E from XIATECH) is based on the transient hot wire technique [37]. The rig is capable of measuring the thermal conductivity of various materials with a accuracy of 3%. For the measurement of specific thermal capacity, we adopted an indirect method, i.e, the thermal probe method [38, 39]. For a thermal probe installed in homogenous soil, the temperature response of soil surrounds the thermal probe is proportional to the soil thermal diffusivity ($k/\rho c$), as can be seen from the basic Fourier heat condition equation in Equation (1). The experimental rig shown in Figure 7 was used to obtain the soil thermal diffusivity of the two different soils by filling only one type of soil in the soil box. The measurement results of soil properties are given in Table 1. The values of soil total bulk density and thermal conductivity are the average values of the three repeated measurements.

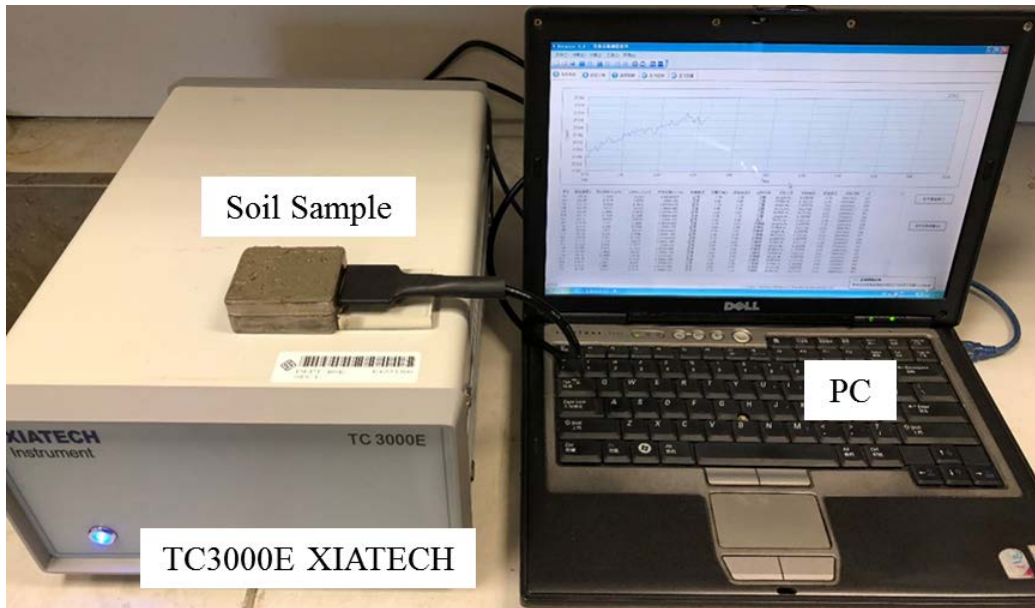


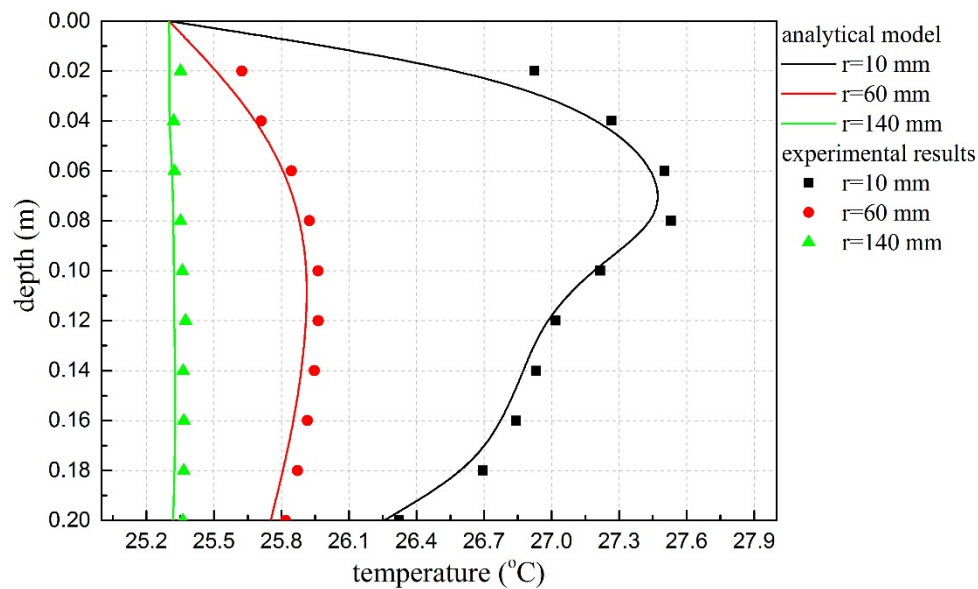
Figure 8 Test rig for soil thermal conductivity measurement

soil layer	bulk density kg/m^3	thermal conductivity $W/(m \cdot K)$	specific thermal capacity $J/(kg \cdot K)$
layer 1 (silt)	1834.6	1.09	1656.57
layer 2 (sand)	1989.1	2.12	1557.83

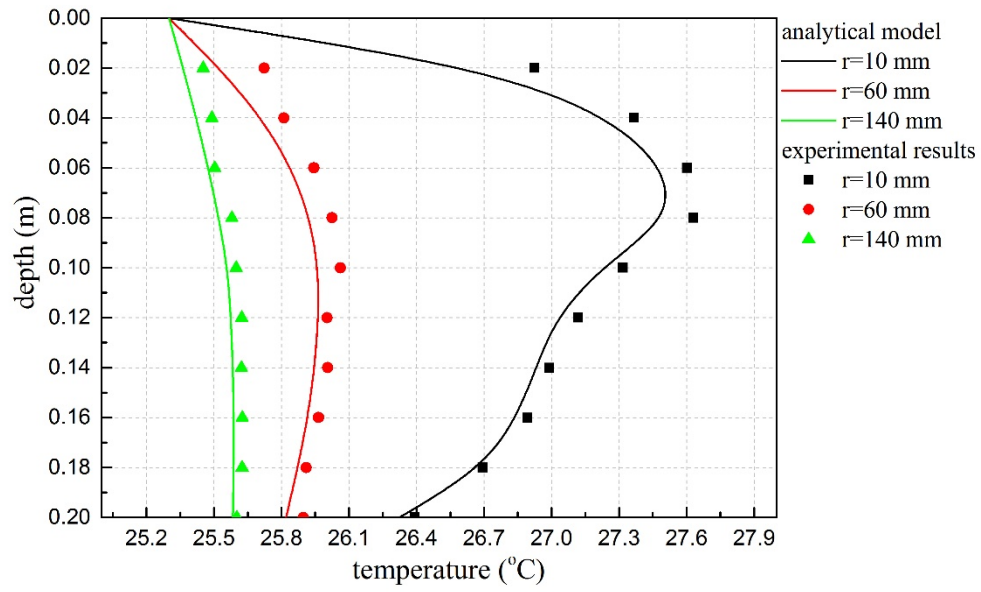
Table 1 Measured soil properties

The room where the experiment was conducted was air-conditioned at about 23.5 °C. Before starting the experiment, the soil was left to stabilize until its initial temperature was the same as the room temperature. The duration of the experiment was 30 days under continuous heating. Due to the limitation of the size of experimental rig, it was expected that the boundary effect caused by the acrylic soil box (the thermal conductivity of the acrylic material is $0.20 W/(m \cdot K)$) would gradually build up and affect the temperature measurement as heat conduct radially with time. Since how significant the boundary effect would affect the temperature measurement was not sure before the experiment, the experiment during lasted for 30 days, which later was found to be long that the temperature had been significant affected. The comparison between the results of the analytical multilayer model and the experiment are shown in Figure 9.

After 24 hours of heating, the temperature profile at the radius of 10 mm measured by resistance thermometers agrees reasonably well with that of analytical model. Temperature rise at the radius of 60 mm is marginal while at $r = 140$ mm, there is barely any temperature rise. Also, after 10 days' heating, the temperature profile at $r = 10$ mm is almost the same with that after 24 hours of heating, meaning that temperature at $r = 10$ mm has reached near steady state after 24 hours of heating. However, temperatures at $r = 60$ mm and $r = 140$ mm continue to rise. At day 10, the differences between the experimental results and that of the analytical model is generally larger than that at day 1. This is probably caused by the boundary effects of the limited soil box. Also, the temperatures near surface is generally larger than that at deeper locations. This is probably caused by the surface boundary effects, since the analytical model has assumed a constant ground surface temperature. In summary, the deviation of temperature profile along the depth of cylindrical heat source was captured experimentally and agrees reasonably well with that of the analytical multilayer cylindrical heat source model.



(a) Day 1



(b) Day 10

Figure 9 Comparisons between analytical model and experimental results

4 Study on effect of layered ground

In this section, temperature solutions in homogeneous and inhomogeneous ground are firstly compared. Then, the thermal interactions between soil layers are analyzed by plotting the temperature profile along the depth of vertical GHE and the heat flux across ground layer interfaces. Finally, the error of using multilayer line heat source model to calculate temperature solutions is analyzed by comparing its results with the results of multilayer cylindrical heat source model.

4.1 Temperature solutions in homogeneous and layered ground

Figure 10 compares the dimensionless temperature solutions on the wall of vertical GHE at different dimensionless times in homogeneous and layered ground. The dimensionless depth of vertical GHE is 200. For a direct comparison of temperature profile along the depth of vertical GHE, the vertical GHE is surrounded by two layers with same thickness but different thermal properties. The parameter values of the four cases compared in Figure 10 are given in Table 2, where α_i and β_i is the thermal conductivity ratio and thermal capacity ratio respectively as defined in Equation (14) and Equation (15). In case 1 and case 2, thermal conductivities in upper and lower layers are opposite (twice the value of the other layer), while the thermal capacities of the two layers are the same. To further analyze the effect of thermal conductivity, the thermal conductivity of upper layer and lower layer is set to be 0.75 and 2.25 respectively while the thermal capacities of the two layers are the same in case 3 in comparison to case 1. In case 4 and case 5, the thermal capacities of upper and lower layers are opposite, while the thermal conductivities of the two layers are the same. For the homogeneous case calculated for comparisons, the values of α and β all equal 1.5 as a mean value of thermal conductivity in the range of the depth of vertical GHE. The comparisons of temperature solutions in layered ground with that in homogeneous ground demonstrate the effects of layered ground on the temperature profile along

vertical GHE.

Figure 10	thermal properties of layered ground			
	α_1	α_2	β_1	β_2
Case 1	1	2	1	1
Case 2	2	1	1	1
Case 3	0.75	2.25	1	1
Case 4	1	1	1	2
case 5	1	1	2	1

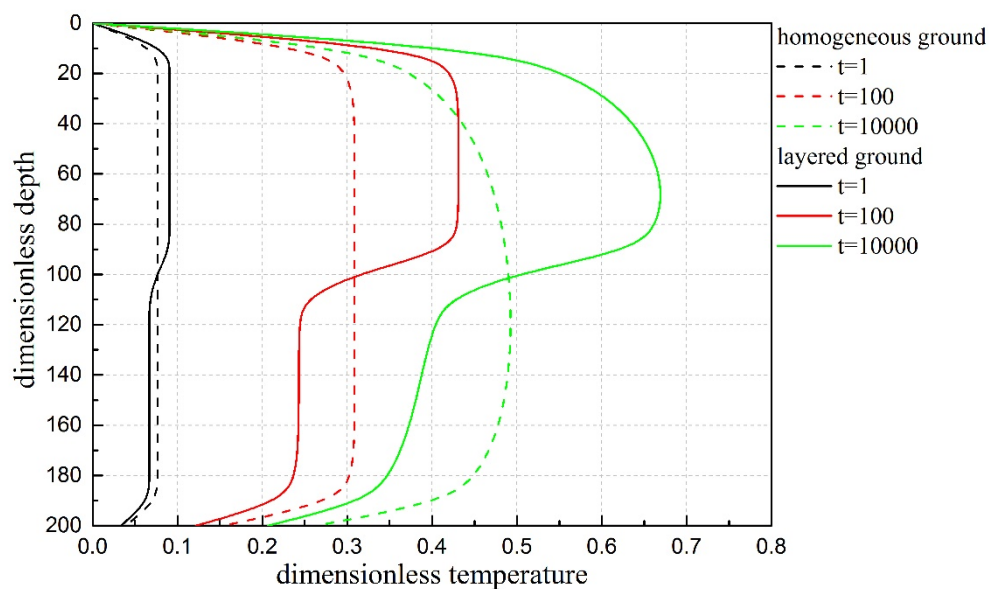
Table 2 Thermal properties of layered ground

In Figure 10 (a) and Figure 10 (b), it can be seen that due to the differences in thermal conductivities, the dimensionless temperatures are significantly different compared with that in homogeneous ground with equivalent thermal conductivity. The differences get larger with time. For case 1, the dimensionless temperature difference at dimensionless time 10000 is 0.20 for upper layer and 0.11 for lower layer respectively. For case 2, the difference is 0.11 and 0.21 respectively. Comparing temperature solutions in layered ground in Figure 10 (a) and Figure 10 (b), it can be found that at relatively early state ($t=1$), the maximal dimensionless temperature is the same, though in different layers. However, the maximal dimensionless temperature in layer 2 in case 2 is about 0.02 higher than that in layer 1 in case 1 at $t=10000$. This is probably caused by the fixed temperature boundary condition of ground surface. When the thermal conductivity of upper soil layer close to ground surface is lower and the resulting temperature is higher, the heat flux through ground surface will also be larger. Therefore, the peak temperature is lower for the case when the upper soil has lower thermal conductivity.

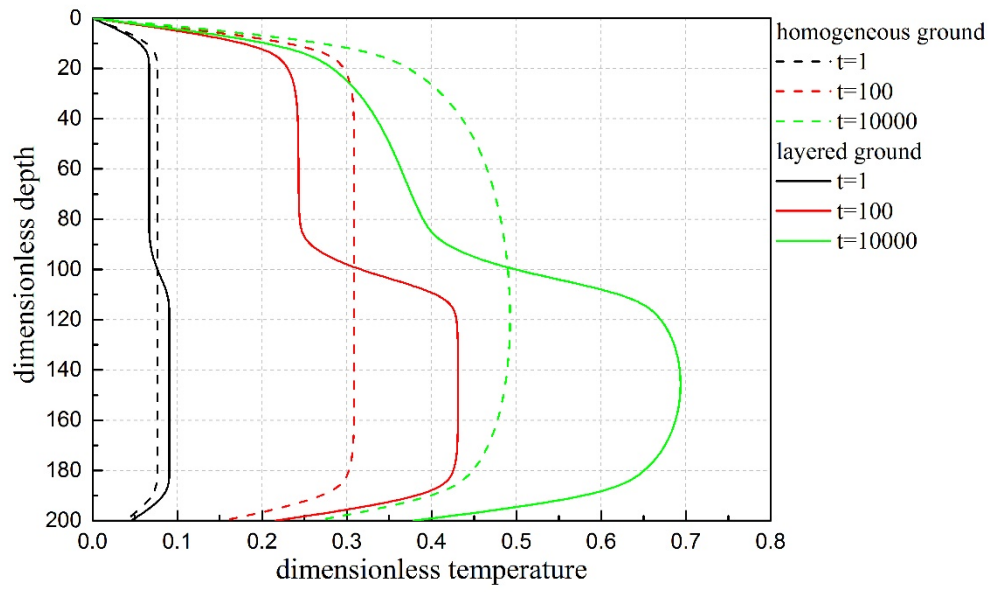
In case 1, the thermal conductivity ratio of lower layer to upper layer is 2. In case 3, the ratio is 3. Comparing corresponding temperature solutions in Figure 10 (a) and Figure 10 (b), it can be seen that at $t=10000$, the maximal temperature difference in upper layer and lower layer is 0.4 and 0.14 respectively, in comparison to 0.2 and 0.11 respectively in case 1. Therefore, the temperature differences would be larger when

thermal conductivity difference between soil layers is larger.

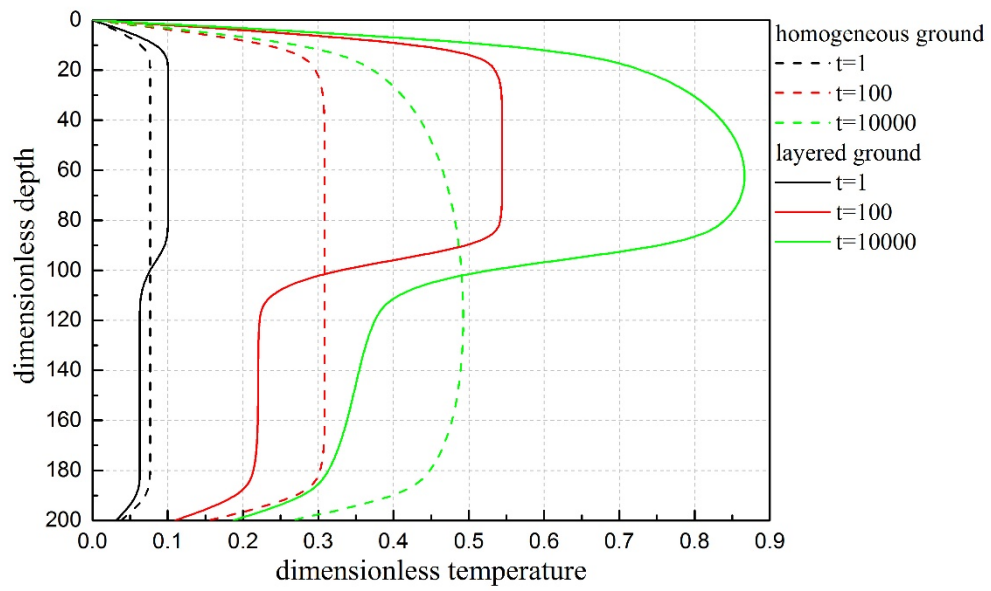
The effects of differences in thermal capacity of layered ground are shown in Figure 10 (c) and Figure 10 (d). Unlike the effects of thermal conductivity, the dimensionless temperature differences would not simply get larger with time. The differences get larger with time in both layers firstly, as can be seen by comparing the temperature profiles at $t=100$ and $t=1$. Then, the differences diminish with time. At $t=10000$, there is almost no difference for both case 3 and case 4, since dimensionless time 10000 is close to steady state. This can be explained by the different physical meaning of thermal conductivity and thermal capacity. While thermal conductivity means the ability to conduct heat, thermal capacity refers to the amount of heat that can be stored in the mass. When the thermal conductivities of the two layers are the same but the thermal capacities are different, the temperature differences would increase first, since after absorbing same amount of heat, the layer with higher thermal capacity would have lower temperature rise. However, the temperature difference would gradually vanish, since there in the long term would be enough released heat for the mass to absorb.



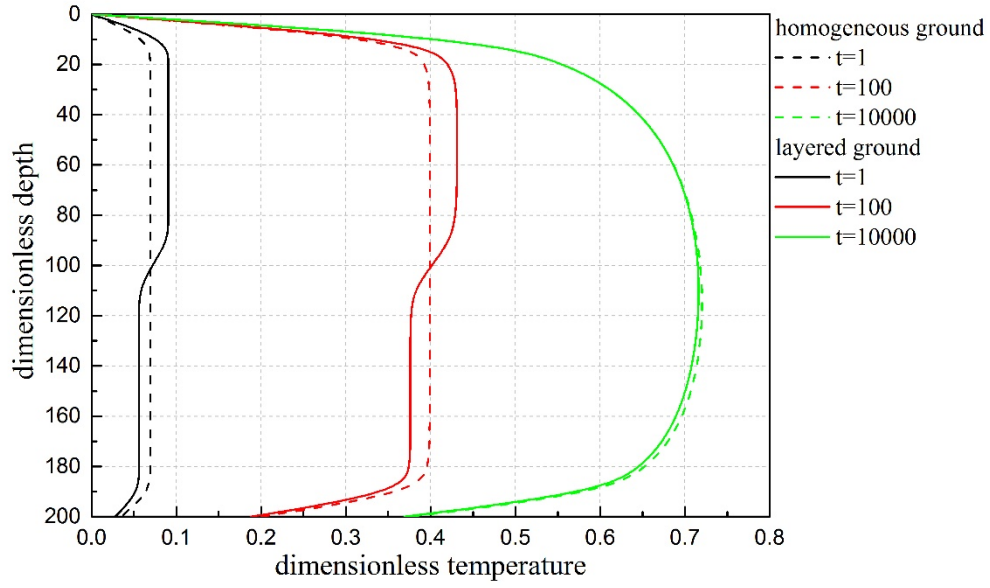
(a) Case 1



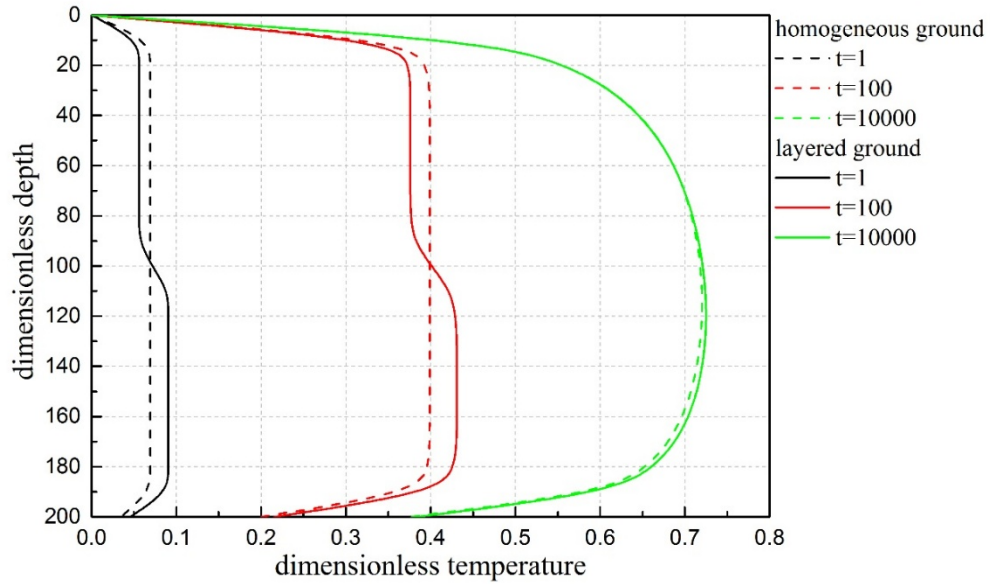
(b) Case 2



(d) Case 3



(c) Case 4



(c) Case 5

Figure 10 Temperature solutions in homogeneous and layered ground

4.2 Thermal interactions between ground layers

4.2.1 Temperature solutions

Considering thermal property differences of layered ground brings about an additional heat transfer process which is not considered in homogeneous models: the thermal interaction between ground layers. This interaction is analyzed by comparing

temperature solutions in two ground layers with different ratios of thermal conductivity, and by plotting the vertical heat flux across ground layers.

As shown in Figure 11, the solid line represents the dimensionless temperature solutions of the case that thermal conductivities of upper layer and lower layer equals 1 and 2 respectively. The dash line stands for the case that thermal conductivities of upper layer and lower layer equals 1 and 3 respectively. Comparing the solid line and dash line at $t=10000$, it is clear that the dimensionless temperature in upper layer is more affected by the lower layer when thermal conductivity ratio is 1:3. The maximal temperature in upper is 0.02 smaller when thermal conductivity ratio is 1:3 compared with 1:2. This is because when the lower layer has higher thermal conductivity, the resulting temperature would be lower. And due to larger temperature difference, the vertical heat flux from upper layer to lower layer would be larger. The vertical heat flux is further analyzed below.

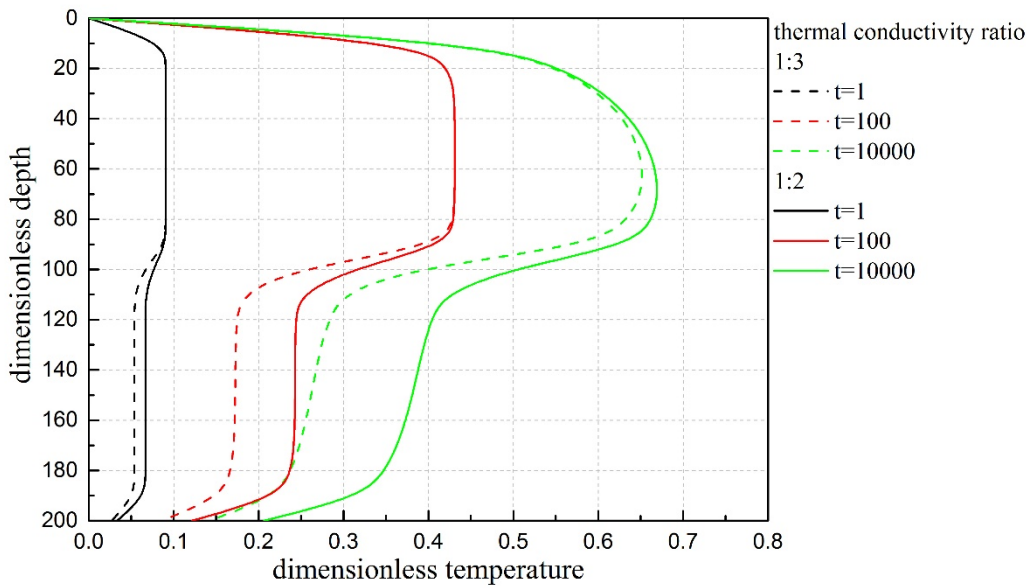


Figure 11 Thermal interaction between ground layers

4.2.2 Vertical Heat flux

One of the advantages of the integral-transform method is that the vertical heat flux across ground layers can be calculated with explicit expressions. For the disk heat source in layer 1, the resulting vertical heat flux across layer interface $\bar{\bar{q}}_z(\varphi, h_1, s)$ has

been given in Equation (31). Integrating $\bar{\bar{q}}_z(\varphi, h_1, s)$ in Equation (31) from 0 to h_1 gives the vertical heat flux across layer interface caused by the separated cylindrical heat source in layer 1:

$$\bar{\bar{q}}_z(\varphi, h_1, s) = \frac{\alpha_2 \gamma_2 \left[\gamma_1^2 (b_1)_{h_1}^2 - (a_1)_{h_1}^2 + (a_1)_{h_1} \right]}{\gamma_1^2 \left[\alpha_2 \gamma_2 (b_1)_{h_1} + \alpha_1 (a_1)_{h_1} \right]} \frac{J_1(\varphi)}{\pi \varphi s} \quad (52)$$

Also, for the disk heat source in layer 2, the resulting vertical heat flux across layer interface $\bar{\bar{q}}_z(\varphi, h_1, s)$ has been given in Equation (41). Integrating $\bar{\bar{q}}_z(\varphi, h_1, s)$ in Equation (41) from 0 to $h_d - h_1$ gives the vertical heat flux across layer interface caused by the separated cylindrical heat source in layer 2:

$$\bar{\bar{q}}_z(\varphi, h_1, s) = - \frac{\alpha_1 (a_1)_{h_1} [1 - \exp[-\gamma_2 (h_d - h_1)]]}{\alpha_1 \gamma_2 (a_1)_{h_1} + \alpha_2 \gamma_2^2 (b_1)_{h_1}} \frac{J_1(\varphi)}{\pi \varphi s} \quad (53)$$

Adding the results calculated by Equations (52) and (53) gives the vertical heat flux across the layer interface caused by the entire cylindrical heat source.

The calculation results are shown in Figure 12. The dark line is the result when the ground is homogeneous (thermal conductivity ratio is 1:1). Clearly, in homogeneous ground, the vertical heat flux is almost zero at depth of h_1 . In contrast, the vertical heat flux gets larger with time in layered ground. And the value is clearly larger when thermal conductivity ratio is larger. This explains the temperature profile in Figure 11 that when the lower layer has larger thermal conductivity, the temperature profile in upper layer is more affected.

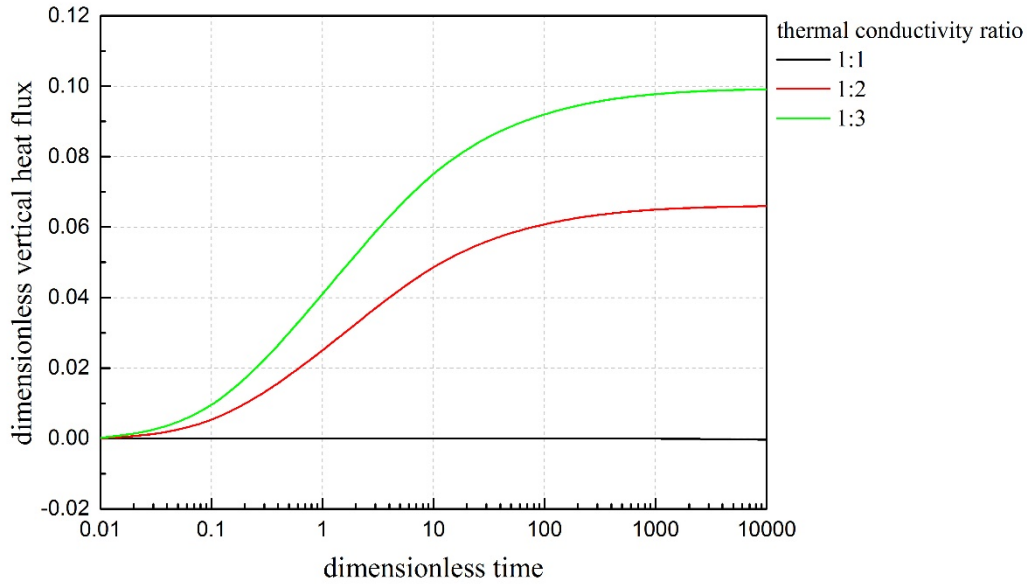


Figure 12 Vertical heat flux across ground layers

Therefore, it can be concluded that thermal interaction between soil layers is determined by two factors: time and thermal conductivity ratio between ground layers. On one hand, a larger thermal conductivity ratio between ground layers results in bigger temperature differences between ground layers, which would cause stronger thermal interaction between soil layers. On the other hand, temperature difference between ground layers increases with time, resulting in stronger vertical heat flux across layer interface in the long term.

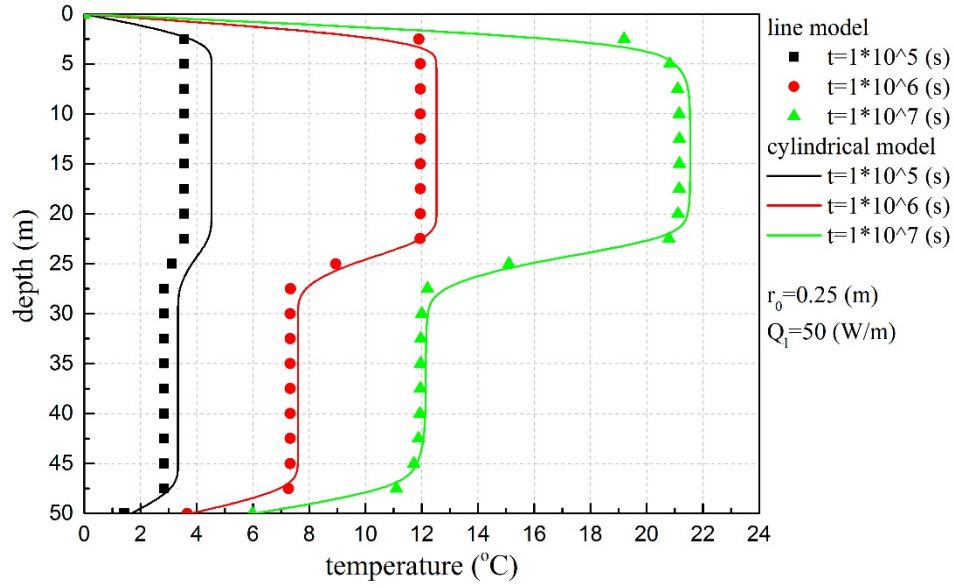
4.3 Error analysis of multilayer line heat source model

The heat source model for vertical GHE assuming a homogeneous ground have improved from line heat source model to cylindrical heat source model. It is generally believed that cylindrical heat source models are more accurate than line heat source models for vertical GHE, since cylindrical models consider the real GHE radius. As most of current multilayer heat source models for vertical GHE are line heat source models, the temperature solutions calculated by multilayer cylindrical and line heat source are compared. Four parameters, i.e., time, thermal conductivity, thermal load, and GHE radius are chosen to study their effects on the error of multilayer cylindrical line heat source independently.

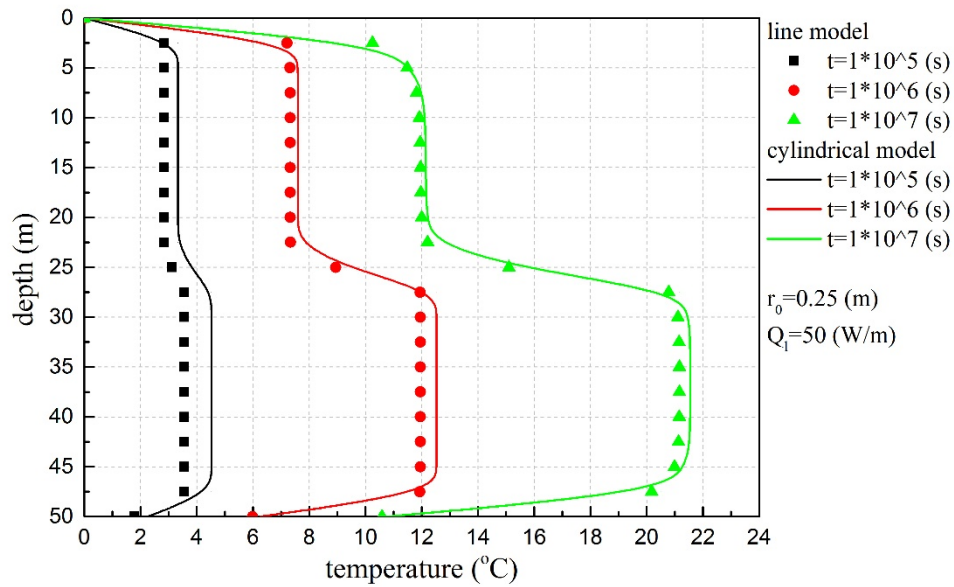
4.3.1 Effect of time and thermal conductivity

In Figure 13 (a), the thermal conductivity of upper layer and lower layer is $1 \text{ W/(m}\cdot\text{K)}$ and $2 \text{ W/(m}\cdot\text{K)}$ respectively, while in Figure 13 (b), the thermal conductivity of the upper layer and lower layer is $1 \text{ W/(m}\cdot\text{K)}$ and $2 \text{ W/(m}\cdot\text{K)}$ respectively. Density and specific thermal capacity for both layers in both figures is 2000 kg/m^3 and $800 \text{ J/(kg}\cdot\text{K)}$ respectively. The temperature rises on the GHE wall at the three different time are compared between multilayer line and cylindrical heat source model. It can be seen in Figure 13 (a) and Figure 13 (b) that the temperature solutions of line source model are always smaller at the three times, but the differences narrow down with time. This can be explained that heat concentrates on the line in line heat source model which neglect the radial dimension of GHE but heat evenly distributes on the cylindrical heat source model which consider the radial dimension of GHE. Therefore, at early stage when heat just travels from the line heat source to the radial location 0.25 m, the values calculated by line heat source are smaller than that calculated by cylindrical heat source. The differences narrow down with time because in the long term, heat would have enough time to fully reach the radial location.

Also, in both Figure 13 (a) and Figure 13 (b), the differences between multilayer line and cylindrical heat source model are larger in layers with smaller thermal conductivity, which is more obvious in early stage at $t = 1 \times 10^5 \text{ s}$. This can also be explained that heat concentrates on the line in line heat source model which neglect the radial dimension of GHE but heat evenly distributes on the cylindrical heat source model which consider the radial dimension of GHE. Therefore, when the thermal conductivity is smaller, it is harder for heat to reach the radial location 0.25 m. So, the difference is larger in the layer with smaller thermal conductivity than in the layer with larger thermal conductivity.



(a)



(b) Effect of time and thermal conductivity

Figure 13 Effect of time and thermal conductivity

4.3.2 Effect of thermal load

Figure 14 compares the temperature differences between multilayer line and cylindrical heat source model when GHE has different thermal loads. The thermal conductivity of upper layer and lower layer is $1 \text{ W/(m} \cdot \text{K)}$ and $2 \text{ W/(m} \cdot \text{K)}$ respectively. Density and specific thermal capacity for both layers is 2000 kg/m^3 and $800 \text{ J/(kg} \cdot \text{K)}$ respectively. It can be seen in Figure 14 that the differences in both

layers are proportional to the difference in thermal load. This can be explained that larger thermal load means larger heat release from the heat source. Therefore, the heat released from the line heat source and transferred to the radial location 0.25 m is less under smaller thermal load than larger thermal load. So, the temperature solutions of line heat source is proportionally smaller to that of cylindrical heat source according to thermal load.

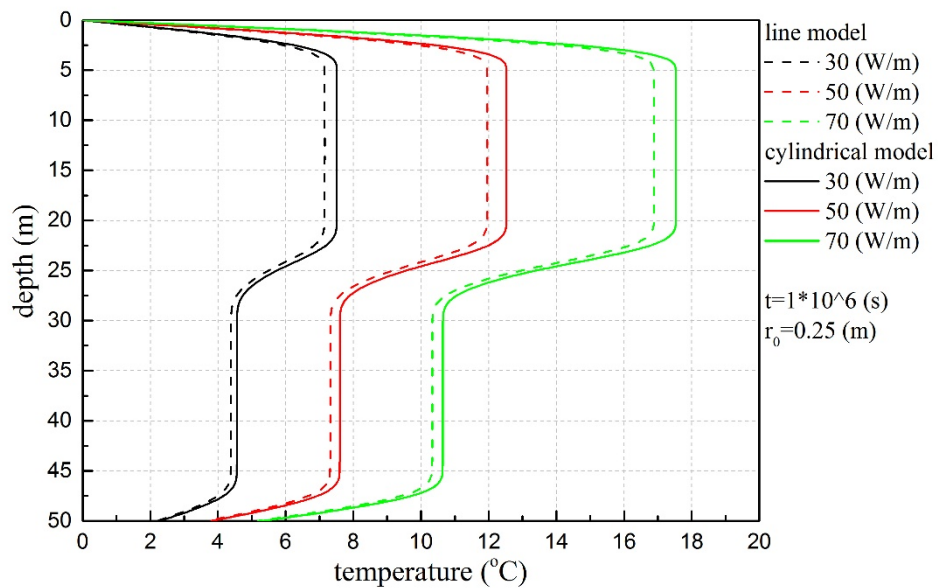


Figure 14 Effect of thermal load

4.3.2 Effect of GHE radius

Figure 15 compares the temperature differences between multilayer line and cylindrical heat source model when GHE has different radiuses. One is 0.25 m and the other is 0.5 m. The thermal conductivity of upper layer and lower layer is $1 \text{ W}/(\text{m} \cdot \text{K})$ and $2 \text{ W}/(\text{m} \cdot \text{K})$ respectively. Density and specific thermal capacity for both layers is $2000 \text{ kg}/\text{m}^3$ and $800 \text{ J}/(\text{kg} \cdot \text{K})$ respectively. Comparing the black solid line and red solid line, it can be found that when GHE radius is 0.25 m, the temperature differences is 0.6°C and 0.3°C in upper layer and lower layer respectively. Comparing the black dashed line and red dashed line, it can be found that when GHE radius is 0.50 m, the temperature differences is also 0.6°C and 0.3°C in upper layer and lower layer respectively. So, the GHE radius has no effect on the temperature differences between

line and cylindrical heat source model. This should be explained that even when line heat source model neglects the radial dimension of GHE, the temperature solutions at the real corresponding radial location are used when conducting the comparisons.

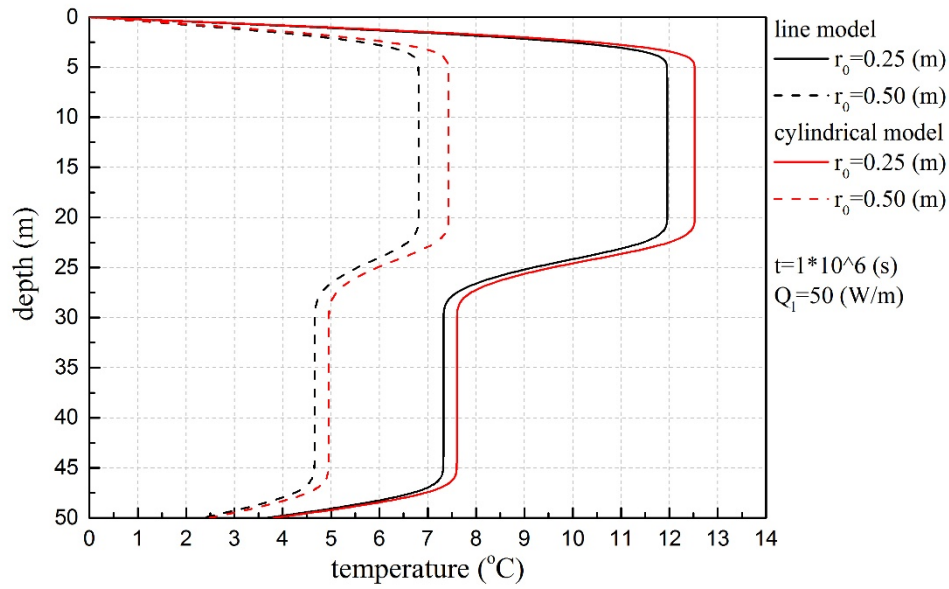


Figure 15 Effect of GHE radius

5 Conclusion

This paper successfully developed a new cylindrical heat source model for vertical GHEs in layered ground by employing the integral-transform method. The new multilayer cylindrical heat source model was validated by model degradation, numerical simulation, and laboratory-scale experiments. Using the new multilayer cylindrical model, temperature solutions of vertical GHE in layered ground were compared with that in homogeneous ground. Temperature profiles on the GHE wall were found to change significantly due to differences in thermal properties between ground layers. Also, differences in thermal property between ground layers were found to result in thermal interaction between ground layers. This interaction was investigated by comparing temperature profiles in two-layer ground with different thermal conductivity ratios and plotting vertical heat flux across layer interface. For larger thermal conductivity ratio between two layers, the temperature difference between the layers and vertical heat flux across the layer interfaces are both larger. Also, the thermal interaction between ground layers was found to increase with time, gradually influencing the temperature in each individual layer.

The error of using a multilayer line heat source model to calculate the temperature solutions of vertical GHE was also studied through comparison with the results from the multilayer cylindrical heat source model. It is demonstrated that as the error diminishes with time. Also, the error is larger in soil layers with smaller thermal conductivity, however, this error near the soil interface would be narrowed down by adjacent layer with larger thermal conductivity due to thermal interactions. In addition, when vertical GHE have higher thermal load, the error of using multilayer line heat source model would also be larger. On the other hand, GHE radius is unlikely to affect the error.

In conclusion, homogeneous heat source models fail to give the real temperature profiles along the depth of vertical GHE in layered soils, and the error may increase with time. Also, compared with multilayer line heat source model, the multilayer

cylindrical heat source model is more accurate to predict temperature solutions for vertical GHEs. This new analytical multilayer heat source model can be an effective quick-calculation tool to consider ground stratification in the design of vertical GHEs.

Acknowledgement:

Partially supported financially by RGC General Research Fund (Project No.: PolyU 152010/15E and PolyU 152184/17E) and PolyU Research Student Attachment Programme 2017/2018.

Appendix A

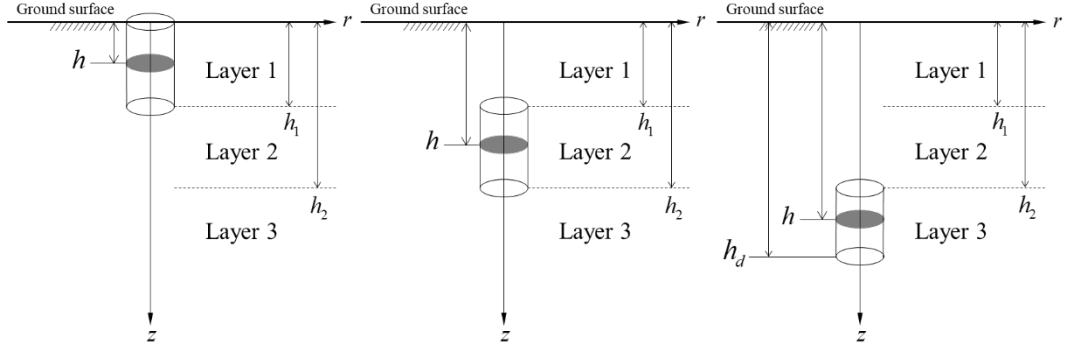


Figure A1 The separated cylindrical heat source in each soil layer

Appendix A.1

For the separated cylindrical heat source in layer 1, the range of disk heat source is $0 < h < h_1$.

Step 1: solving for heat flux and temperature on boundaries: $\bar{\bar{q}}_z(\varphi, 0, s)$, $\bar{\bar{T}}(\varphi, h_1, s)$, $\bar{\bar{q}}_z(\varphi, h_1, s)$, $\bar{\bar{T}}(\varphi, h_2, s)$, $\bar{\bar{q}}_z(\varphi, h_2, s)$

According to Equation (26), at $z = \infty$

$$\bar{\bar{T}}(\varphi, \infty, s) = (a_3)_{\infty} \bar{\bar{T}}(\varphi, h_2, s) - \left(\frac{b_3}{\alpha_3} \right)_{\infty} \bar{\bar{q}}_z(\varphi, h_2, s) \quad (\text{A1})$$

With boundary conditions, Equation (A1) gives:

$$\alpha_3 \gamma_3 \bar{\bar{T}}(\varphi, h_2, s) = \bar{\bar{q}}_z(\varphi, h_2, s) \quad (\text{A2})$$

Also, at $z = h_2$

$$\begin{aligned} \bar{\bar{T}}(\varphi, h_2, s) &= (a_2)_{h_2} \bar{\bar{T}}(\varphi, h_1, s) - \left(\frac{b_2}{\alpha_2} \right)_{h_2} \bar{\bar{q}}_z(\varphi, h_1, s) \\ \bar{\bar{q}}_z(\varphi, h_2, s) &= -(b_2)_{h_2} \alpha_2 \gamma_2^2 \bar{\bar{T}}(\varphi, h_1, s) + (a_2)_{h_2} \bar{\bar{q}}_z(\varphi, h_1, s) \end{aligned} \quad (\text{A3})$$

At $z = h_1$

$$\begin{aligned} \bar{\bar{T}}(\varphi, h_1, s) &= -\left(\frac{b_1}{\alpha_1} \right)_{h_1} \bar{\bar{q}}_z(\varphi, 0, s) - \frac{J_1(\varphi) dh}{\pi \varphi s} \left(\frac{b_1}{\alpha_1} \right)_{h_1-h} \\ \bar{\bar{q}}_z(\varphi, h_1, s) &= (a_1)_{h_1} \bar{\bar{q}}_z(\varphi, 0, s) + \frac{J_1(\varphi) dh}{\pi \varphi s} (a_1)_{h_1-h} \end{aligned} \quad (\text{A4})$$

With Equations (A2) to (A4), $\bar{\bar{q}}_z(\varphi, 0, s)$ can be obtained.

$$\bar{\bar{q}}_z(\varphi, 0, s) = -C_1 \frac{J_1(\varphi)dh}{\pi\varphi s} \quad (\text{A5})$$

$$\text{Where } C = \frac{\left[\alpha_3 \gamma_3 \left(\frac{b_2}{\alpha_2} \right)_{h_2} + (a_2)_{h_2} \right]}{\left[\alpha_3 \gamma_3 (a_2)_{h_2} + \alpha_2 \gamma_2^2 (b_2)_{h_2} \right]}, \text{ and } C_1 = \frac{\left(\frac{b_1}{\alpha_1} \right)_{h_1-h} + C (a_1)_{h_1-h}}{\left(\frac{b_1}{\alpha_1} \right)_{h_1} + C (a_1)_{h_1}}.$$

And $\bar{\bar{T}}(\varphi, h_1, s), \bar{\bar{q}}_z(\varphi, h_1, s), \bar{\bar{T}}(\varphi, h_2, s), \bar{\bar{q}}_z(\varphi, h_2, s)$ can also be obtained respectively.

$$\bar{\bar{T}}(\varphi, h_1, s) = \left[\left(\frac{b_1}{\alpha_1} \right)_{h_1} C_1 - \left(\frac{b_1}{\alpha_1} \right)_{h_1-h} \right] \frac{J_1(\varphi)dh}{\pi\varphi s} \quad (\text{A6})$$

$$\bar{\bar{q}}_z(\varphi, h_1, s) = \left[-(a_1)_{h_1} C_1 + (a_1)_{h_1-h} \right] \frac{J_1(\varphi)dh}{\pi\varphi s} \quad (\text{A7})$$

$$\begin{aligned} \bar{\bar{T}}(\varphi, h_2, s) = & \left\{ (a_2)_{h_2} \left[\left(\frac{b_1}{\alpha_1} \right)_{z=h_1} C_1 - \left(\frac{b_1}{\alpha_1} \right)_{h_1-h} \right] - \left(\frac{b_2}{\alpha_2} \right)_{h_2} \left[-(a_1)_{h_1} C_1 + (a_1)_{h_1-h} \right] \right\} \frac{J_1(\varphi)dh}{\pi\varphi s} \quad (\text{A8}) \end{aligned}$$

$$\begin{aligned} \bar{\bar{q}}_z(\varphi, h_2, s) = & \left\{ -(b_2)_{h_2} \alpha_2 \gamma_2^2 \left[\left(\frac{b_1}{\alpha_1} \right)_{h_1} C_1 - \left(\frac{b_1}{\alpha_1} \right)_{h_1-h} \right] + (a_2)_{h_2} \left[-(a_1)_{h_1} C_1 + (a_1)_{h_1-h} \right] \right\} \frac{J_1(\varphi)dh}{\pi\varphi s} \quad (\text{A9}) \end{aligned}$$

Step 2: solution of disk heat source in all layers

Using the solution of $\bar{\bar{q}}_z(\varphi, 0, s), \bar{\bar{T}}(\varphi, h_1, s), \bar{\bar{q}}_z(\varphi, h_1, s), \bar{\bar{T}}(\varphi, h_2, s), \bar{\bar{q}}_z(\varphi, h_2, s)$, the solution of disk heat source in each layer can be obtained. According to Equation (26), in layer 1 ($0 < z < h_1$)

For $z < h < h_1$

$$\bar{\bar{T}}(\varphi, z, s) = \frac{b_1}{\alpha_1} C_1 \frac{J_1(\varphi)dh}{\pi\varphi s} \quad (\text{A10})$$

For $h < z < h_1$

$$\bar{\bar{T}}(\varphi, z, s) = \left[\frac{b_1}{\alpha_1} C_1 - \left(\frac{b_1}{\alpha_1} \right)_{z-h} \right] \frac{J_1(\varphi) dh}{\pi \varphi s} \quad (\text{A11})$$

In layer 2 ($h_1 < z < h_2$)

$$\bar{\bar{T}}(\varphi, z, s) = \left\{ a_2 \left[\left(\frac{b_1}{\alpha_1} \right)_{h_1} C_1 - \left(\frac{b_1}{\alpha_1} \right)_{h_1-h} \right] - \frac{b_2}{\alpha_2} \left[-(a_1)_{h_1} C_1 + (a_1)_{h_1-h} \right] \right\} \frac{J_1(\varphi) dh}{\pi \varphi s} \quad (\text{A12})$$

In layer 3 ($h_2 < z$)

$$\bar{\bar{T}}(\varphi, z, s) = \left\{ a_3 \left\{ \begin{aligned} &\left(a_2 \right)_{h_2} \left[\left(\frac{b_1}{\alpha_1} \right)_{h_1} C_1 - \left(\frac{b_1}{\alpha_1} \right)_{h_1-h} \right] \\ &- \left(\frac{b_2}{\alpha_2} \right)_{h_2} \left[-(a_1)_{h_1} C_1 + (a_1)_{h_1-h} \right] \end{aligned} \right\} - \frac{b_3}{\alpha_3} \left\{ \begin{aligned} &- (b_2)_{h_2} \alpha_2 \gamma_2^2 \left[\left(\frac{b_1}{\alpha_1} \right)_{h_1} C_1 - \left(\frac{b_1}{\alpha_1} \right)_{h_1-h} \right] \\ &+ (a_2)_{h_2} \left[-(a_1)_{h_1} C_1 + (a_1)_{h_1-h} \right] \end{aligned} \right\} \right\} \frac{J_1(\varphi) dh}{\pi \varphi s} \quad (\text{A13})$$

Step 3: solution of separated cylindrical heat source

For $0 < z < h_1$, adding up integration of Equation (A11) from 0 to z and Equation (A10) from z to h_1 , and the result gives

$$\bar{\bar{T}}(\varphi, z, s) = \left[\frac{\frac{b_1}{\alpha_1} (E_1 + C E_2)}{\left(\frac{b_1}{\alpha_1} \right)_{h_1} + C (a_1)_{h_1}} - E_3 \right] \frac{J_1(\varphi)}{\pi \varphi s} \quad (\text{A14})$$

For $h_1 < z < h_2$, integrating Equation (A12) from 0 to h_1 gives

$$\bar{\bar{T}}(\varphi, z, s) = \left\{ \frac{\left[a_2 \left(\frac{b_1}{\alpha_1} \right)_{h_1} + \frac{b_2}{\alpha_2} (a_1)_{h_1} \right]}{\left(\frac{b_1}{\alpha_1} \right)_{h_1} + C (a_1)_{h_1}} (E_1 + C E_2) - a_2 E_1 - \frac{b_2}{\alpha_2} E_2 \right\} \frac{J_1(\varphi)}{\pi \varphi s} \quad (\text{A15})$$

For $h_2 < z$, integration Equation (A13) from 0 to h_1 gives

$$\begin{aligned} \bar{\bar{T}}(\varphi, z, s) = & \left\{ \frac{a_3 \left[(a_2)_{h_2} \left(\frac{b_1}{\alpha_1} \right)_{h_1} + \left(\frac{b_2}{\alpha_2} \right)_{h_2} (a_1)_{h_1} \right]}{\left(\frac{b_1}{\alpha_1} \right)_{h_1} + C(a_1)_{h_1}} + \right. \\ & \left. \frac{\frac{b_3}{\alpha_3} \left[(b_2)_{h_2} \alpha_2 \gamma_2^2 \left(\frac{b_1}{\alpha_1} \right)_{h_1} + (a_2)_{h_2} (a_1)_{h_1} \right]}{\left(\frac{b_1}{\alpha_1} \right)_{h_1} + C(a_1)_{h_1}} \right\} (E_1 + CE_2) \frac{J_1(\varphi)}{\pi \varphi s} \\ & - \left\{ \left[a_3 (a_2)_{h_2} + \frac{b_3}{\alpha_3} (b_2)_{h_2} \alpha_2 \gamma_2^2 \right] E_1 + \left[a_3 \left(\frac{b_2}{\alpha_2} \right)_{h_2} + \frac{b_3}{\alpha_3} (a_2)_{h_2} \right] E_2 \right\} \frac{J_1(\varphi)}{\pi \varphi s} \end{aligned} \quad (A16)$$

And expressions of E_1, E_2, E_3 are

$$E_1 = \int_0^{h_1} \left(\frac{b_1}{\alpha_1} \right)_{h_1-h} dh = \frac{1}{2\alpha_1 \gamma_1^2} [-2 + \exp(\gamma_1 h_1) + \exp(-\gamma_1 h_1)]$$

$$E_2 = \int_0^{h_1} (a_1)_{h_1-h} dh = \frac{1}{2\gamma_1} [\exp(\gamma_1 h_1) - \exp(-\gamma_1 h_1)]$$

$$E_3 = \int_0^z \left(\frac{b_1}{\alpha_1} \right)_{z-h} dh = \frac{1}{2\alpha_1 \gamma_1^2} [-2 + \exp(\gamma_1 z) + \exp(-\gamma_1 z)]$$

Appendix A.2

For the separated cylindrical heat source in layer 2, the range of disk heat source is

$$h_1 < h < h_2.$$

Step 1: solving for heat flux and temperature on boundaries: $\bar{\bar{q}}_z(\varphi, 0, s)$, $\bar{\bar{T}}(\varphi, h_1, s)$,

$$\bar{\bar{q}}_z(\varphi, h_1, s), \bar{\bar{T}}(\varphi, h_2, s), \bar{\bar{q}}_z(\varphi, h_2, s)$$

According to Equation (26), at $z = \infty$

$$\bar{\bar{T}}(\varphi, \infty, s) = (a_3)_\infty \bar{\bar{T}}(\varphi, h_2, s) - \left(\frac{b_3}{\alpha_3} \right)_\infty \bar{\bar{q}}_z(\varphi, h_2, s) \quad (A17)$$

With boundary conditions, Equation (A17) gives:

$$\alpha_3 \gamma_3 \bar{\bar{T}}(\varphi, h_2, s) = \bar{\bar{q}}_z(\varphi, h_2, s) \quad (\text{A18})$$

Also, at $z = h_2$

$$\begin{aligned} \bar{\bar{T}}(\varphi, h_2, s) &= (a_2)_{h_2} \bar{\bar{T}}(\varphi, h_1, s) - \left(\frac{b_2}{\alpha_2} \right)_{h_2} \bar{\bar{q}}_z(\varphi, h_1, s) - \frac{J_1(\varphi)dh}{\pi\varphi s} \left(\frac{b_2}{\alpha_2} \right)_{h_2-h} \\ \bar{\bar{q}}_z(\varphi, h_2, s) &= -(b_2)_{h_2} \alpha_2 \gamma_2^2 \bar{\bar{T}}(\varphi, h_1, s) + (a_2)_{h_2} \bar{\bar{q}}_z(\varphi, h_1, s) + \frac{J_1(\varphi)dh}{\pi\varphi s} (a_2)_{h_2-h} \end{aligned} \quad (\text{A19})$$

At $z = h_1$

$$\begin{aligned} \bar{\bar{T}}(\varphi, h_1, s) &= - \left(\frac{b_1}{\alpha_1} \right)_{h_1} \bar{\bar{q}}_z(\varphi, 0, s) \\ \bar{\bar{q}}_z(\varphi, h_1, s) &= (a_1)_{h_1} \bar{\bar{q}}_z(\varphi, 0, s) \end{aligned} \quad (\text{A20})$$

With Equations (A18) to (A20), $\bar{\bar{q}}_z(\varphi, 0, s)$ can be obtained.

$$\bar{\bar{q}}_z(\varphi, 0, s) = -C_2 \frac{J_1(\varphi)dh}{\pi\varphi s} \quad (\text{A21})$$

$$\text{Where } C_2 = \frac{1}{\left(\frac{b_1}{\alpha_1} \right)_{h_1} + C(a_1)_{h_1} \left[\frac{\alpha_3 \gamma_3 \left(\frac{b_2}{\alpha_2} \right)_{h_2-h} + (a_2)_{h_2-h}}{\alpha_3 \gamma_3 (a_2)_{h_2} + \alpha_2 \gamma_2^2 (b_2)_{h_2}} \right]}.$$

And $\bar{\bar{T}}(\varphi, h_1, s)$, $\bar{\bar{q}}_z(\varphi, h_1, s)$, $\bar{\bar{T}}(\varphi, h_2, s)$, $\bar{\bar{q}}_z(\varphi, h_2, s)$ can also be obtained respectively.

$$\bar{\bar{T}}(\varphi, h_1, s) = \left(\frac{b_1}{\alpha_1} \right)_{h_1} C_2 \frac{J_1(\varphi)dh}{\pi\varphi s} \quad (\text{A22})$$

$$\bar{\bar{q}}_z(\varphi, h_1, s) = -(a_1)_{h_1} C_2 \frac{J_1(\varphi)dh}{\pi\varphi s} \quad (\text{A23})$$

$$\bar{\bar{T}}(\varphi, h_2, s) = \left\{ \left[(a_2)_{h_2} \left(\frac{b_1}{\alpha_1} \right)_{h_1} + \left(\frac{b_2}{\alpha_2} \right)_{h_2} (a_1)_{h_1} \right] C_2 - \left(\frac{b_2}{\alpha_2} \right)_{h_2-h} \right\} \frac{J_1(\varphi)dh}{\pi\varphi s} \quad (\text{A24})$$

$$\bar{\bar{q}}_z(\varphi, h_2, s) = \left\{ \left[-(b_2)_{h_2} \alpha_2 \gamma_2^2 \left(\frac{b_1}{\alpha_1} \right)_{h_1} - (a_2)_{h_2} (a_1)_{h_1} \right] C_2 + (a_2)_{h_2-h} \right\} \frac{J_1(\varphi)dh}{\pi\varphi s} \quad (\text{A25})$$

Step 2: solution of disk heat source in all layers

Using the solution of $\bar{\bar{q}}_z(\varphi, 0, s), \bar{\bar{T}}(\varphi, h_1, s), \bar{\bar{q}}_z(\varphi, h_1, s), \bar{\bar{T}}(\varphi, h_2, s), \bar{\bar{q}}_z(\varphi, h_2, s)$, the solution of disk heat source in each layer can be obtained. According to Equation (26), in layer 1 ($0 < z < h_1$)

$$\bar{\bar{T}}(\varphi, z, s) = \frac{b_1}{\alpha_1} C_2 \frac{J_1(\varphi) dh}{\pi \varphi s} \quad (\text{A26})$$

In layer 2 ($h_1 < z < h_2$)

For $h_1 < z < h$

$$\bar{\bar{T}}(\varphi, z, s) = \left[a_2 \left(\frac{b_1}{\alpha_1} \right)_{h_1} + \frac{b_2}{\alpha_2} (a_1)_{h_1} \right] C_2 \frac{J_1(\varphi) dh}{\pi \varphi s} \quad (\text{A27})$$

For $h < z < h_2$

$$\bar{\bar{T}}(\varphi, z, s) = \left\{ \left[a_2 \left(\frac{b_1}{\alpha_1} \right)_{h_1} + \frac{b_2}{\alpha_2} (a_1)_{h_1} \right] C_2 - \left(\frac{b_2}{\alpha_2} \right)_{z-h} \right\} \frac{J_1(\varphi) dh}{\pi \varphi s} \quad (\text{A28})$$

In layer 3 ($h_2 < z$)

$$\begin{aligned} \bar{\bar{T}}(\varphi, z, s) = & \left\{ a_3 \left\{ \left[\left(a_2 \right)_{h_2} \left(\frac{b_1}{\alpha_1} \right)_{h_1} + \left(\frac{b_2}{\alpha_2} \right)_{h_2} (a_1)_{h_1} \right] C_2 - \left(\frac{b_2}{\alpha_2} \right)_{h_2-h} \right\} \right. \\ & \left. - \frac{b_3}{\alpha_3} \left\{ - (b_2)_{h_2} \alpha_2 \gamma_2^2 \left(\frac{b_1}{\alpha_1} \right)_{h_1} - (a_2)_{h_2} (a_1)_{h_1} \right\} C_2 + (a_2)_{h_2-h} \right\} \frac{J_1(\varphi) dh}{\pi \varphi s} \end{aligned} \quad (\text{A29})$$

Step 3: solution of separated cylindrical heat source

For $0 < z < h_1$, integrating Equation (A26) from 0 to $h_2 - h_1$ gives

$$\bar{\bar{T}}(\varphi, z, s) = \frac{\frac{b_1}{\alpha_1} (\alpha_3 \gamma_3 E_4 + E_5) \frac{J_1(\varphi)}{\pi \varphi s}}{\left[\left(\frac{b_1}{\alpha_1} \right)_{h_1} + C (a_1)_{h_1} \right] \left[\alpha_3 \gamma_3 (a_2)_{h_2} + \alpha_2 \gamma_2^2 (b_2)_{h_2} \right]} \quad (\text{A30})$$

For $h_1 < z < h_2$, adding up integration of Equation (A28) from 0 to $z - h_1$ and Equation

(A27) from $z - h_1$ to $h_2 - h_1$, and the result gives

$$\bar{\bar{T}}(\varphi, z, s) = \left\{ \frac{\left[a_2 \left(\frac{b_1}{\alpha_1} \right)_{h_1} + \frac{b_2}{\alpha_2} (a_1)_{h_1} \right] (\alpha_3 \gamma_3 E_4 + E_5)}{\left[\left(\frac{b_1}{\alpha_1} \right)_{h_1} + C(a_1)_{h_1} \right] [\alpha_3 \gamma_3 (a_2)_{h_2} + \alpha_2 \gamma_2^2 (b_2)_{h_2}]} - E_6 \right\} \frac{J_1(\varphi)}{\pi \varphi s} \quad (\text{A31})$$

For $h_2 < z$, integrating Equation (A29) from 0 to $h_2 - h_1$ gives

$$\begin{aligned} \bar{\bar{T}}(\varphi, z, s) = & \left\{ \frac{a_3 \left[(a_2)_{h_2} \left(\frac{b_1}{\alpha_1} \right)_{h_1} + \left(\frac{b_2}{\alpha_2} \right)_{h_2} (a_1)_{h_1} \right]}{\left[\left(\frac{b_1}{\alpha_1} \right)_{h_1} + C(a_1)_{h_1} \right] [\alpha_3 \gamma_3 (a_2)_{h_2} + \alpha_2 \gamma_2^2 (b_2)_{h_2}]} + \right. \\ & \left. \frac{\frac{b_3}{\alpha_3} \left[(b_2)_{h_2} \alpha_2 \gamma_2^2 \left(\frac{b_1}{\alpha_1} \right)_{h_1} + (a_2)_{h_2} (a_1)_{h_1} \right]}{\left[\left(\frac{b_1}{\alpha_1} \right)_{h_1} + C(a_1)_{h_1} \right] [\alpha_3 \gamma_3 (a_2)_{h_2} + \alpha_2 \gamma_2^2 (b_2)_{h_2}]} \right\} (\alpha_3 \gamma_3 E_4 + E_5) \frac{J_1(\varphi)}{\pi \varphi s} \quad (\text{A32}) \\ & - \left(a_3 E_4 + \frac{b_3}{\alpha_3} E_5 \right) \frac{J_1(\varphi)}{\pi \varphi s} \end{aligned}$$

And expressions of E_4, E_5, E_6 are

$$E_4 = \int_0^{h_2-h_1} \left(\frac{b_2}{\alpha_2} \right)_{h_2-h} dh = \frac{1}{2\alpha_2 \gamma_2^2} \{ \exp[\gamma_2(h_2 - h_1)] + \exp[-\gamma_2(h_2 - h_1)] - 2 \}$$

$$E_5 = \int_0^{h_2-h_1} (a_2)_{h_2-h} dh = \frac{1}{2\gamma_2} \{ \exp[\gamma_2(h_2 - h_1)] - \exp[-\gamma_2(h_2 - h_1)] \}$$

$$E_6 = \int_0^{z-h_1} \left(\frac{b_2}{\alpha_2} \right)_{z-h} dh = \frac{1}{2\alpha_2 \gamma_2^2} \{ \exp[\gamma_2(z - h_1)] + \exp[-\gamma_2(z - h_1)] - 2 \}$$

Appendix A.3

For the separated cylindrical heat source in layer 3, the range of disk heat source is

$$h_2 < h < h_d.$$

Step 1: solving for heat flux and temperature on boundaries: $\bar{\bar{q}}_z(\varphi, 0, s)$, $\bar{\bar{T}}(\varphi, h_1, s)$,

$$\bar{\bar{q}}_z(\varphi, h_1, s), \bar{\bar{T}}(\varphi, h_2, s), \bar{\bar{q}}_z(\varphi, h_2, s)$$

According to Equation (26), at $z = \infty$

$$\bar{\bar{T}}(\varphi, \infty, s) = (a_3)_{\infty} \bar{\bar{T}}(\varphi, h_2, s) - \left(\frac{b_3}{\alpha_3} \right)_{\infty} \bar{\bar{q}}_z(\varphi, h_2, s) - \frac{J_1(\varphi)dh}{\pi\varphi s} \left(\frac{b_3}{\alpha_3} \right)_{\infty-h} \quad (\text{A33})$$

With boundary conditions, Equation (A33) gives:

$$0 = -\alpha_3 \gamma_3 \bar{\bar{T}}(\varphi, h_2, s) + \bar{\bar{q}}_z(\varphi, h_2, s) + \frac{J_1(\varphi)dh}{\pi\varphi s} \exp(-\gamma_3 h) \quad (\text{A34})$$

Also, at $z = h_2$

$$\begin{aligned} \bar{\bar{T}}(\varphi, h_2, s) &= (a_2)_{h_2} \bar{\bar{T}}(\varphi, h_1, s) - \left(\frac{b_2}{\alpha_2} \right)_{h_2} \bar{\bar{q}}_z(\varphi, h_1, s) \\ \bar{\bar{q}}_z(\varphi, h_2, s) &= -(b_2)_{h_2} \alpha_2 \gamma_2^2 \bar{\bar{T}}(\varphi, h_1, s) + (a_2)_{h_2} \bar{\bar{q}}_z(\varphi, h_1, s) \end{aligned} \quad (\text{A35})$$

At $z = h_1$

$$\begin{aligned} \bar{\bar{T}}(\varphi, h_1, s) &= -\left(\frac{b_1}{\alpha_1} \right)_{h_1} \bar{\bar{q}}_z(\varphi, 0, s) \\ \bar{\bar{q}}_z(\varphi, h_1, s) &= (a_1)_{h_1} \bar{\bar{q}}_z(\varphi, 0, s) \end{aligned} \quad (\text{A36})$$

With Equations (A34) to (A36), $\bar{\bar{q}}_z(\varphi, 0, s)$ can be obtained.

$$\bar{\bar{q}}_z(\varphi, 0, s) = -C_3 \frac{J_1(\varphi)dh}{\pi\varphi s} \exp(-\gamma_3 h) \quad (\text{A37})$$

Where $C_3 = \frac{1}{\left[\left(\frac{b_1}{\alpha_1} \right)_{h_1} + C(a_1)_{h_1} \right] \left[\alpha_3 \gamma_3 (a_2)_{h_2} + \alpha_2 \gamma_2^2 (b_2)_{h_2} \right]}$.

And $\bar{\bar{T}}(\varphi, h_1, s), \bar{\bar{q}}_z(\varphi, h_1, s), \bar{\bar{T}}(\varphi, h_2, s), \bar{\bar{q}}_z(\varphi, h_2, s)$ can also be obtained respectively.

$$\bar{\bar{T}}(\varphi, h_1, s) = \left(\frac{b_1}{\alpha_1} \right)_{h_1} C_3 \frac{J_1(\varphi)dh}{\pi\varphi s} \exp(-\gamma_3 h) \quad (\text{A38})$$

$$\bar{\bar{q}}_z(\varphi, h_1, s) = -(a_1)_{h_1} C_3 \frac{J_1(\varphi)dh}{\pi\varphi s} \exp(-\gamma_3 h) \quad (\text{A39})$$

$$\bar{\bar{T}}(\varphi, h_2, s) = \left[(a_2)_{h_2} \left(\frac{b_1}{\alpha_1} \right)_{h_1} + \left(\frac{b_2}{\alpha_2} \right)_{h_2} (a_1)_{h_1} \right] C_3 \frac{J_1(\varphi) dh}{\pi \varphi s} \exp(-\gamma_3 h) \quad (\text{A40})$$

$$\bar{\bar{q}}_z(\varphi, h_2, s) = \left[-(b_2)_{h_2} \alpha_2 \gamma_2^2 \left(\frac{b_1}{\alpha_1} \right)_{h_1} - (a_2)_{h_2} (a_1)_{h_1} \right] C_3 \frac{J_1(\varphi) dh}{\pi \varphi s} \exp(-\gamma_3 h) \quad (\text{A41})$$

Step 2: solution of disk heat source in all layers

Using the solution of $\bar{\bar{q}}_z(\varphi, 0, s)$, $\bar{\bar{T}}(\varphi, h_1, s)$, $\bar{\bar{q}}_z(\varphi, h_1, s)$, $\bar{\bar{T}}(\varphi, h_2, s)$, $\bar{\bar{q}}_z(\varphi, h_2, s)$, the solution of disk heat source in each layer can be obtained. According to Equation (26), in layer 1 ($0 < z < h_1$)

$$\bar{\bar{T}}(\varphi, z, s) = \frac{b_1}{\alpha_1} C_3 \frac{J_1(\varphi) dh}{\pi \varphi s} \exp(-\gamma_3 h) \quad (\text{A42})$$

In layer 2 ($h_1 < z < h_2$)

$$\bar{\bar{T}}(\varphi, z, s) = \left[a_2 \left(\frac{b_1}{\alpha_1} \right)_{h_1} + \frac{b_2}{\alpha_2} (a_1)_{h_1} \right] C_3 \frac{J_1(\varphi) dh}{\pi \varphi s} \exp(-\gamma_3 h) \quad (\text{A43})$$

In layer 3 ($h_2 < z$)

For $h_2 < z < h$

$$\bar{\bar{T}}(\varphi, z, s) = \left\{ a_3 \left[(a_2)_{h_2} \left(\frac{b_1}{\alpha_1} \right)_{h_1} + \left(\frac{b_2}{\alpha_2} \right)_{h_2} (a_1)_{h_1} \right] C_3 \right. \\ \left. - \frac{b_3}{\alpha_3} \left[-(b_2)_{h_2} \alpha_2 \gamma_2^2 \left(\frac{b_1}{\alpha_1} \right)_{h_1} - (a_2)_{h_2} (a_1)_{h_1} \right] C_3 \right\} \frac{J_1(\varphi) dh}{\pi \varphi s} \exp(-\gamma_3 h) \quad (\text{A44})$$

For $h < z$

$$\begin{aligned} \bar{\bar{T}}(\varphi, z, s) = & \left\{ a_3 \left[(a_2)_{h_2} \left(\frac{b_1}{\alpha_1} \right)_{h_1} + \left(\frac{b_2}{\alpha_2} \right)_{h_2} (a_1)_{h_1} \right] C_3 \right. \\ & \left. - \frac{b_3}{\alpha_3} \left[-(b_2)_{h_2} \alpha_2 \gamma_2^2 \left(\frac{b_1}{\alpha_1} \right)_{h_1} - (a_2)_{h_2} (a_1)_{h_1} \right] C_3 \right\} \frac{J_1(\varphi) dh}{\pi \varphi s} \exp(-\gamma_3 h) \\ & - \left(\frac{b_3}{\alpha_3} \right)_{z-h} \frac{J_1(\varphi) dh}{\pi \varphi s} \end{aligned} \quad (\text{A45})$$

Step 3: solution of separated cylindrical heat source

For $0 < z < h_1$, integrating Equation (A42) from 0 to $h_d - h_2$ gives

$$\bar{\bar{T}}(\varphi, z, s) = \frac{\frac{b_1}{\alpha_1} E_7 \frac{J_1(\varphi)}{\pi \varphi s}}{\left[\left(\frac{b_1}{\alpha_1} \right)_{h_1} + C(a_1)_{h_1} \right] \left[\alpha_3 \gamma_3 (a_2)_{h_2} + \alpha_2 \gamma_2^2 (b_2)_{h_2} \right]} \quad (\text{A46})$$

For $h_1 < z < h_2$, integrating Equation (A43) from 0 to $h_d - h_2$ gives

$$\bar{\bar{T}}(\varphi, z, s) = \frac{\left[a_2 \left(\frac{b_1}{\alpha_1} \right)_{h_1} + \frac{b_2}{\alpha_2} (a_1)_{h_1} \right] E_7 \frac{J_1(\varphi)}{\pi \varphi s}}{\left[\left(\frac{b_1}{\alpha_1} \right)_{h_1} + C(a_1)_{h_1} \right] \left[\alpha_3 \gamma_3 (a_2)_{h_2} + \alpha_2 \gamma_2^2 (b_2)_{h_2} \right]} \quad (\text{A47})$$

For $h_2 < z < h_d$, adding up integration of Equation (A45) from 0 to $z - h_2$ and Equation

(A44) from $z - h_2$ to $h_d - h_2$, and the result gives

$$\bar{\bar{T}}(\varphi, z, s) = \left\{ \begin{array}{l} \frac{a_3 \left[(a_2)_{h_2} \left(\frac{b_1}{\alpha_1} \right)_{h_1} + \left(\frac{b_2}{\alpha_2} \right)_{h_2} (a_1)_{h_1} \right]}{\left[\left(\frac{b_1}{\alpha_1} \right)_{h_1} + C(a_1)_{h_1} \right] \left[\alpha_3 \gamma_3 (a_2)_{h_2} + \alpha_2 \gamma_2^2 (b_2)_{h_2} \right]} + \\ \frac{\frac{b_3}{\alpha_3} \left[(b_2)_{h_2} \alpha_2 \gamma_2^2 \left(\frac{b_1}{\alpha_1} \right)_{h_1} + (a_2)_{h_2} (a_1)_{h_1} \right]}{\left[\left(\frac{b_1}{\alpha_1} \right)_{h_1} + C(a_1)_{h_1} \right] \left[\alpha_3 \gamma_3 (a_2)_{h_2} + \alpha_2 \gamma_2^2 (b_2)_{h_2} \right]} \end{array} \right\} E_7 \frac{J_1(\varphi)}{\pi \varphi s} - E_8 \frac{J_1(\varphi)}{\pi \varphi s} \quad (\text{A48})$$

For $h_d < z$, integrating Equation (A45) from 0 to $h_d - h_2$ gives

$$\bar{\bar{T}}(\varphi, z, s) = \left\{ \begin{array}{l} \frac{a_3 \left[(a_2)_{h_2} \left(\frac{b_1}{\alpha_1} \right)_{h_1} + \left(\frac{b_2}{\alpha_2} \right)_{h_2} (a_1)_{h_1} \right]}{\left[\left(\frac{b_1}{\alpha_1} \right)_{h_1} + C(a_1)_{h_1} \right] \left[\alpha_3 \gamma_3 (a_2)_{h_2} + \alpha_2 \gamma_2^2 (b_2)_{h_2} \right]} + \\ \frac{\frac{b_3}{\alpha_3} \left[(b_2)_{h_2} \alpha_2 \gamma_2^2 \left(\frac{b_1}{\alpha_1} \right)_{h_1} + (a_2)_{h_2} (a_1)_{h_1} \right]}{\left[\left(\frac{b_1}{\alpha_1} \right)_{h_1} + C(a_1)_{h_1} \right] \left[\alpha_3 \gamma_3 (a_2)_{h_2} + \alpha_2 \gamma_2^2 (b_2)_{h_2} \right]} \end{array} \right\} E_7 \frac{J_1(\varphi)}{\pi \varphi s} - E_9 \frac{J_1(\varphi)}{\pi \varphi s} \quad (\text{A49})$$

And expressions of E_7, E_8, E_9 are

$$E_7 = \int_0^{h_d - h_2} \exp(-\gamma_3 h) dh = -\frac{1}{\gamma_3} \{ \exp[-\gamma_3 (h_d - h_2)] - 1 \}$$

$$E_8 = \int_0^{z - h_2} \left(\frac{b_3}{\alpha_3} \right)_{z-h} dh = \frac{1}{2\alpha_3 \gamma_3^2} \{ \exp[\gamma_3 (z - h_2)] + \exp[-\gamma_3 (z - h_2)] - 2 \}$$

$$E_9 = \int_0^{h_d - h_2} \left(\frac{b_3}{\alpha_3} \right)_{z-h} dh = \frac{1}{2\alpha_3 \gamma_3^2} \left\{ \begin{array}{l} -\exp[\gamma_3 (z - h_d)] + \exp[\gamma_3 (z - h_2)] \\ -\exp[-\gamma_3 (z - h_d)] + \exp[-\gamma_3 (z - h_2)] \end{array} \right\}$$

The final solution of the entire cylindrical heat source can be obtained by adding up the temperature in each layer by the three separated cylindrical heat sources. For $0 < z < h_1$, adding up Equations (A14), (A30), and (A46). For $h_1 < z < h_2$, adding up

Equations (A15), (A31), and (A47). For $h_2 < z < h_d$, adding up Equations (A16), (A32), and (A48). For $h_d < z$, adding up Equations (A16), (A32), and (A49).

Reference

1. Wang, C., et al., *Modeling and optimal operation of community integrated energy systems: A case study from China*. Applied Energy, 2018. **230**: p. 1242-1254.
2. Wouters, C., E.S. Fraga, and A.M. James, *An energy integrated, multi-microgrid, MILP (mixed-integer linear programming) approach for residential distributed energy system planning—a South Australian case-study*. Energy, 2015. **85**: p. 30-44.
3. Miglani, S., K. Orehounig, and J. Carmeliet, *Integrating a thermal model of ground source heat pumps and solar regeneration within building energy system optimization*. Applied Energy, 2018. **218**: p. 78-94.
4. Xia, L., et al., *A model-based optimal control strategy for ground source heat pump systems with integrated solar photovoltaic thermal collectors*. Applied energy, 2018. **228**: p. 1399-1412.
5. Self, S.J., B.V. Reddy, and M.A. Rosen, *Geothermal heat pump systems: Status review and comparison with other heating options*. Applied Energy, 2013. **101**: p. 341-348.
6. Yang, H., P. Cui, and Z. Fang, *Vertical-borehole ground-coupled heat pumps: A review of models and systems*. Applied energy, 2010. **87**(1): p. 16-27.
7. Reuss, M., *The use of borehole thermal energy storage (BTES) systems*, in *Advances in Thermal Energy Storage Systems*. 2015, Elsevier. p. 117-147.
8. Loveridge, F. and W. Powrie, *Temperature response functions (G-functions) for single pile heat exchangers*. Energy, 2013. **57**: p. 554-564.
9. Loveridge, F. and W. Powrie, *2D thermal resistance of pile heat exchangers*. Geothermics, 2014. **50**: p. 122-135.
10. Cecinato, F. and F.A. Loveridge, *Influences on the thermal efficiency of energy piles*. Energy, 2015. **82**: p. 1021-1033.
11. Murphy, K.D., J.S. McCartney, and K.S. Henry, *Evaluation of thermo-mechanical and thermal behavior of full-scale energy foundations*. Acta Geotechnica, 2015. **10**(2): p. 179-195.
12. Park, S., et al., *Relative constructability and thermal performance of cast-in-place concrete energy pile: Coil-type GHEX (ground heat exchanger)*. Energy, 2015. **81**: p. 56-66.
13. Park, S., et al., *Effect of thermal interference on energy piles considering various configurations of heat exchangers*. Energy and Buildings, 2019. **199**: p. 381-401.
14. Li, M. and A.C. Lai, *Review of analytical models for heat transfer by vertical ground heat exchangers (GHEs): A perspective of time and space scales*. Applied Energy, 2015. **151**: p. 178-191.
15. Lu, S., et al., *An improved model for predicting soil thermal conductivity from water content at room temperature*. Soil Science Society of America Journal, 2007. **71**(1): p. 8-14.
16. Dong, Y., J.S. McCartney, and N. Lu, *Critical review of thermal conductivity models for unsaturated soils*. Geotechnical and Geological Engineering, 2015. **33**(2): p. 207-221.
17. Lu, N. and Y. Dong, *Closed-form equation for thermal conductivity of unsaturated soils at room temperature*. Journal of Geotechnical and Geoenvironmental Engineering, 2015. **141**(6): p. 04015016.

18. Brandon, T. and J. Mitchell, *Factors influencing thermal resistivity of sands*. Journal of Geotechnical Engineering, 1989. **115**(12): p. 1683-1698.
19. Başer, T. and McCartney, J.S. (2018). "Transient performance evaluation of solar thermal energy storage in a geothermal borehole array." *Renewable Energy*. doi.org/10.1016/j.renene.2018.11.012.
20. Li, W., et al., *Experimental investigations of the heat load effect on heat transfer of ground heat exchangers in a layered subsurface*. Geothermics, 2019. **77**: p. 75-82.
21. Guo, Y., G. Zhang, and S. Liu, *Investigation on the thermal response of full-scale PHC energy pile and ground temperature in multi-layer strata*. Applied Thermal Engineering, 2018. **143**: p. 836-848.
22. Luo, J., et al., *Analysis on performance of borehole heat exchanger in a layered subsurface*. Applied Energy, 2014. **123**: p. 55-65.
23. Florides, G.A., P. Christodoulides, and P. Pouloupatis, *Single and double U-tube ground heat exchangers in multiple-layer substrates*. Applied energy, 2013. **102**: p. 364-373.
24. Abdelaziz, S.L., et al., *Multilayer finite line source model for vertical heat exchangers*. Geothermics, 2014. **51**: p. 406-416.
25. Erol, S. and B. François, *Multilayer analytical model for vertical ground heat exchanger with groundwater flow*. Geothermics, 2018. **71**: p. 294-305.
26. Wang, D., et al., *Numerical and analytical analysis of groundwater influence on the pile geothermal heat exchanger with cast-in spiral coils*. Applied energy, 2015. **160**: p. 705-714.
27. Park, S., et al., *Effect of borehole material on analytical solutions of the heat transfer model of ground heat exchangers considering groundwater flow*. Energies, 2016. **9**(5): p. 318.
28. Hu, J., *An improved analytical model for vertical borehole ground heat exchanger with multiple-layer substrates and groundwater flow*. Applied Energy, 2017. **202**: p. 537-549.
29. Zhou, G., Y. Zhou, and D. Zhang, *Analytical solutions for two pile foundation heat exchanger models in a double-layered ground*. Energy, 2016. **112**: p. 655-668.
30. Man, Y., et al., *A new model and analytical solutions for borehole and pile ground heat exchangers*. International Journal of Heat and Mass Transfer, 2010. **53**(13-14): p. 2593-2601.
31. Poularikas, A.D., *Transforms and applications handbook*. 2010: CRC press.
32. Korn, G.A. and T.M. Korn, *Mathematical handbook for scientists and engineers: definitions, theorems, and formulas for reference and review*. 2000: Courier Corporation.
33. Abate, J. and W. Whitt, *A unified framework for numerically inverting Laplace transforms*. INFORMS Journal on Computing, 2006. **18**(4): p. 408-421.
34. Villinger, H., *Solving cylindrical geothermal problems using the Gaver-Stehfest inverse Laplace transform*. Geophysics, 1985. **50**(10): p. 1581-1587.
35. Baddour, N. and U. Chouinard, *Theory and operational rules for the discrete Hankel transform*. JOSA A, 2015. **32**(4): p. 611-622.
36. LEUTENEGGER, M.,
<https://documents.epfl.ch/users/l/le/leuteneg/www/MATLABToolbox/HankelTransform.html>.
37. http://www.xiatech.com.cn/en/products_list.asp?ID=17.
38. *IEEE Guide for Soil Thermal Resistivity Measurements*, " in IEEE Std 442-1981 , vol., no.,

pp.1-16, 12 May 1981.

- 39.Naidu, A.D. and D.N. Singh, *A generalized procedure for determining thermal resistivity of soils*. International Journal of Thermal Sciences, 2004. **43**(1): p. 43-51.